POLITECNICO DI TORINO

Master's Degree in Communications Engineering

Master's Degree Thesis

Performance Analysis of O-band PAM4 Short-Reach IM/DD Systems for Inter-Datacenter Applications

Supervisors
Prof. Andrea Carena
Dr. Ann Margareth Rosa Brusin

Candidate
Alessandra Leo
s319003

2024-2025

Acknowledgements

This thesis marks the conclusion of an important chapter in my academic journey, and I would like to take a moment to acknowledge those who have contributed to it.

I am profoundly grateful to my supervisors, Andrea Carena and Ann Margareth Rosa Brusin, whose guidance, expertise and broad vision have been a constant source of inspiration. They have helped me to strengthen my technical competences and to cultivate a mindset focused on identifying the essence of problems while abstracting the necessary tools to solve them.

I also wish to thank my friends, with whom I have shared these years. Their presence has made this period more enjoyable and truly worth living.

Finally, I owe my deepest gratitude to my family. Their patience, trust and unwavering support have been the foundation of my growth and every achievement in this work is theirs.

Abstract

In recent years, due to the rapid increase in global traffic and the widespread adoption of artificial intelligence (AI) applications and large language models (LLMs), the expansion of data centers has accelerated significantly, with annual growth rates reaching approximately 27% since 2017 [9] . Similar to modern communication networks, data communication (datacom) systems are primarily based on optical fiber technologies because of their large bandwidth, low signal attenuation, and strong resistance to electromagnetic interference and environmental factors.

Today, the goal in inter-datacenter environments is to achieve high-speed data transmission (1.6 Tb/s and above) over short distances, typically in the range of 2–10 km. For cost-related reasons, these systems rely on solutions in the form of Pulse Amplitude Modulation (PAM) combined with direct detection (DD). However, compared to coherent systems, which offer higher spectral efficiency, IM-DD systems require higher symbol rates and larger channel spacings to reach such elevated bit rates.

Recent studies, for example [3], have renewed interest in the O-band for inter-datacenter transmissions, primarily due to its low chromatic dispersion (0 ps/nm/km at 1310 nm) compared to the C-band. This thesis focuses on evaluating the performance of IM-DD systems operating in the O-band with Wavelength Division Multiplexing (WDM) architectures, employing a high symbol rate of 112 GBd and a channel spacing of 400 GHz.

Through simulations, this work analyzes the principal factors that degrade transmission performance, including intersymbol interference (ISI) and chromatic dispersion (CD), in order to better understand their impact on data quality and system reliability. By extracting meaningful insights, this thesis aims to contribute to the optimization of short-reach optical communication systems designed for next-generation high-speed data centers.

Contents

List of Figures

List of Tables

Acronyms

IM-DD Intensity-Modulation Direct-Detection

WDM Wavelength Division Multiplexing

DSP Digital Signal Processing

SPM Self-Phase Modulation

XPM Cross-Phase Modulation

FWM Four-Wave Mixing

ISI Inter-Symbol Interference

CPU Central Processing Unit

GPU Graphics Processing Unit

Chapter 1

Introduction

The recent growth of data center traffic continues to accelerate, driven by the expansion of cloud services and by ongoing research and technological developments aimed at supporting this trend.
Data centers are large-scale infrastructures designed to host computing, networking and storage resources that store, process and distribute data for cloud computing, web services, artificial intelligence applications and massive data processing. They are engineered for high computational density, reliability, scalability, energy efficiency and strong physical and logical security.

In addition to the internal networks that interconnect servers and devices within a single data center, inter-data center links connect multiple data centers across metropolitan, regional and even global distances. These links require extremely high capacity, low latency and strong reliability to enable data replication, load balancing, problem recovery and efficient service delivery close to end users.

IM-DD (Intensity Modulation with Direct Detection) systems represent the simplest and most cost-effective solution for short-reach optical communication links, such as those used in modern data centers. With this technology, the information is encoded directly in the intensity of the optical signal, and the receiver detects the optical power using a photodiode, without the need for a local oscillator or the complex phase recovery DSP employed in coherent systems. This makes IM-DD systems simpler, cheaper, and less power-hungry compared to coherent technology.

In these short-reach systems, used in modern data centers, PAM4 transmission has become the dominant solution thanks to its superior spectral efficiency, which enables higher capacity without increasing the channel bandwidth. This modulation format is now at the core of the latest IEEE 802.3 Ethernet standards, allowing current data rates of 100 Gb/s, 400 Gb/s, and 800 Gb/s through multi-lane architectures based on 50 Gb/s and 100 Gb/s PAM4 per-lane signaling [6], [5] and [2]. Interfaces such as 100GBASE-SR and DR, 400GBASE-SR8, DR4, and FR4, together with the emerging 800GBASE specifications under IEEE 802.3df, support typical short-reach fiber distances,from a few tens of meters on multimode fiber to around 2 km on single-mode fiber, while

ensuring low latency, high reliability, and reduced power consumption [6], [7] and [4]. The adoption of PAM4 for these applications is widely documented in recent optical-communication literature [5], [8] and reflects the need to accommodate the rapid growth of data-center traffic highlighted in industry analyses such as the Cisco Global Cloud Index [12]. These standards represent the current state of the art in high-speed optical interconnects for intra-data center networks and pave the way for next-generation 1.6 Tb/s modules based on 200 Gb/s per-lane PAM4 technology. The next goal is to achieve 1.6 Tb/s and beyond, which exacerbates bandwidth limitations and chromatic dispersion effects, even in the O-band, specifically chosen for its near-zero dispersion region.

1.1 Goal and Structure of the Project

The primary objective of this thesis is to investigate the linear and nonlinear effects that influence the performance of O-band IM-DD WDM transmission systems, that require higher symbol rates and larger channel spacing to reach such elevated bit rates as 1.6 Tb/s. Through simulation-based analysis, this work evaluates how linear and nonlinear interactions jointly affect overall system performance.

As we aim for higher symbol rates, channel bandwidths must be increased, which leads to operating farther from the zero-dispersion wavelength. This results in greater chromatic dispersion, which can be particularly problematic in WDM systems using multilevel amplitude modulation formats like PAM4, where dispersion acts as a low-pass filter and induces intersymbol interference (ISI). Moreover, operating near the zero-dispersion wavelength enhances the impact of nonlinear mixing effects, especially at high launch powers. Understanding these interactions is crucial for designing scalable, high-performance short-reach optical communication systems tailored for next-generation data centers.

1.2 Simulator Description and Setup

The implemented simulator is an object-oriented architecture developed in MATLAB composed of three main blocks: the transmitter, the optical channel and the DSP-based receiver. Each block models the corresponding physical subsystem of a high-speed multi-span WDM optical communication link. The following subsections describe these components with more details.

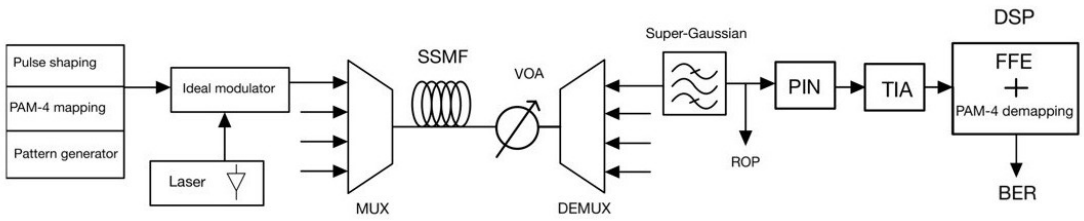

Figure 1.1: PAM-4 Optical Communication System Diagram

1.2.1 Transmitter

At the transmitter, a random sequence of symbols is generated to emulate realistic data traffic and these symbols are mapped onto a four level pulse amplitude modulation (PAM4) format using Gray coding to minimize the bit-error probability.
The symbol sequence length is 2^{16}, with the number of pattern repetition equal to 3.

Using 4 WDM channels spaced by 400 GHz, each channel transmits at a symbol rate of 112 Gbaud with a central wavelength of 1310 nm. The corresponding Nyquist bandwidth for this symbol rate is 134.4 GHz. The electrical signal is pulse-shaped using a root-raised-cosine (RRC) filter with a roll-off factor of 0.2.

The PAM-4 waveform is then filtered by a third order Bessel low-pass filter with a 50 GHz cutoff frequency, modeling the bandwidth limitations of the transmitter, while maintaining a nearly linear phase response to prevent waveform distortion. After pulse shaping, the signal passes through a laser source.

Four wavelength division multiplexed (WDM) channels are combined using an optical multiplexer with 400 GHz spacing, including a realistic insertion loss of 3.5 dB.

1.2.2 Channel

The optical channel models the physical fiber link and its associated linear and nonlinear impairments. The multiplexed WDM signal propagates through a span of standard single-mode fiber (SSMF) operating in the O-band, where chromatic dispersion is close to zero. In this wavelength region, dispersion effects are minimal; however, there are nonlinear phenomena such as self-phase modulation (SPM) or cross-phase modulation (XPM) and especially four-wave mixing (FWM).

The channel parameters include fiber attenuation, Kerr nonlinearity, and amplified spontaneous emission (ASE) noise introduced by an optical amplifier with a realistic noise figure.

Two fiber lengths are considered in the simulations: 10 km and 2 km, both with an attenuation coefficient of 0.35 dB/km, yielding total losses of 3.5 dB and 0.7 dB respectively. The dispersion parameter is $D = 0$ ps/(nm km), and the dispersion slope is $S = 0.09$ ps/(nm^2 km).
The nonlinear coefficient is $\gamma = 1.87$ W^{-1}km^{-1}, resulting in strong expected FWM contributions.

1.2.3 Receiver

After passing through a variable optical attenuator (VOA), which is required to evaluate the variations of the received optical power (ROP), the received signal is demultiplexed (DEMUX) to separate the desired WDM channel. The selected channel is then detected using a direct-detection front-end, where a photodiode converts the instantaneous optical power into an electrical current. This current is subsequently amplified and filtered by the receiver electronics, which include an eighth-order Butterworth low-pass filter with

an 80 GHz cutoff frequency. This filtering introduces intersymbol interference (ISI) and models the response of the transimpedance amplifier (TIA).

The resulting waveform is processed by a digital signal processing (DSP) chain that includes equalization. A linear feed-forward equalizer (FFE), based on the least-mean-square (LMS) algorithm, is used to compensate for bandwidth limitations and intersymbol interference (ISI). Bit decisions are then made, and performance metrics such as the bit-error rate (BER) are computed to assess the system performance.

The thesis is structured into five chapters. Chapter 1 introduces the system model together with the simulation environment, providing the basis for the subsequent analyses. Chapter 2 presents the theoretical background of the experiment, with particular attention to both linear and nonlinear effects. Chapter 3 reports the results of the simulation campaign, including the comparison between CPU and GPU implementations of the simulator, and extends the analysis to chromatic dispersion and its interaction with nonlinear effects in high rates PAM4 transmission within the O-band. Chapter 4 describes the experimental simulations, focusing on the introduction of a dispersion compensating fiber (DCF) within the system and its impact on performance. Finally, Chapter 5 summarizes the main findings and presents the overall conclusions of the work.

Chapter 2

Theoretical background

2.1 Chromatic dispersion

Chromatic Dispersion in IM-DD system is one of the most critical impairments and it's important to understand its impact for system design and optimization. It is a phenomenon caused by fiber impurities that makes the different frequency components of the optical signal travel at different group velocities, resulting in temporal pulse spreading.

In the frequency domain, the electric field at position z and angular frequency ω can be expressed as

$$E(z,\omega) = E(0,\omega)e^{-\alpha z}e^{-j\beta(\omega)z},$$

where α is the attenuation coefficient and $\beta(\omega)$ is the propagation constant that is a function of frequency ω.

$\beta(\omega)$ is usually expanded in a Taylor series centered at the carrier angular frequency ω_0:

$$\beta(\omega) = \beta_0 + \beta_1(\omega-\omega_0) + \frac{\beta_2}{2!}(\omega-\omega_0)^2 + \frac{\beta_3}{3!}(\omega-\omega_0)^3 + \frac{\beta_4}{4!}(\omega-\omega_0)^4 + \cdots$$

Each term in this series represents a physical effect:

$$\beta_0 = \beta(\omega_0), \quad \text{corresponds to a phase delay.} \tag{2.1}$$

$$\beta_1 = \left.\frac{d\beta}{d\omega}\right|_{\omega=\omega_0}, \quad \text{group velocity} \tag{2.2}$$

$$\beta_2 = \left.\frac{d^2\beta}{d\omega^2}\right|_{\omega=\omega_0}, \quad \text{chromatic dispersion.} \tag{2.3}$$

$$\beta_3 = \left.\frac{d^3\beta}{d\omega^3}\right|_{\omega=\omega_0}, \quad \text{third-order dispersion.} \tag{2.4}$$

$$\beta_4 = \left.\frac{d^4\beta}{d\omega^4}\right|_{\omega=\omega_0}, \quad \text{fourth-order dispersion.} \tag{2.5}$$

The angular frequency offset is defined as:

$$\Delta\omega = 2\pi(f - f_0) = 2\pi\,\Delta f.$$

The *fiber transfer function* in the frequency domain is:

$$H(\omega, z) = \exp\left[-\frac{\alpha z}{2} + j\beta(\omega)z\right].$$

Since attenuation acts as a nearly constant scaling factor over the bandwidth of the modulated optical signal, it can be neglected when analyzing chromatic dispersion effects. The Taylor expansion of $\beta(\omega)$ up to the third order gives:

$$H(\omega, z) = \exp\left[j\beta_0 z + j\beta_1(\omega - \omega_0)z + j\frac{\beta_2}{2}(\omega - \omega_0)^2 z + j\frac{\beta_3}{6}(\omega - \omega_0)^3 z\right].$$

Thus, the effective transfer function becomes:

$$H_{\text{eff}}(\Omega, z) = e^{-j\beta_1\Omega z} \cdot e^{-j\frac{\beta_2}{2}\Omega^2 z} \cdot e^{-j\frac{\beta_3}{6}\Omega^3 z}.$$

This formula focuses on the dispersion effects that actually distort the signal. To better study it, there should be a focus only on the second order term of the dispersion formula for the moment.

$$H_{\text{eff}}(\Omega, z) \approx e^{-j\frac{\beta_2}{2}\Omega^2 z}.$$

The group delay is expressed as:

$$\boxed{\tau_g(f) = 2\pi\beta_2(f - f_0)z.}$$

Hence, the group delay varies linearly with frequency, indicating that different spectral components of the optical signal experience different propagation times that is the fundamental cause of chromatic dispersion.

The differential group delay between two frequencies separated by Δf is:

$$\Delta\tau_g = 2\pi\beta_2\,\Delta f\,z.$$

Starting from:

$$\omega = \frac{2\pi c}{\lambda}.$$

Taking the differential:

$$d\omega = -\frac{2\pi c}{\lambda^2}\,d\lambda.$$

Thus, the derivative operator transforms as:

$$\frac{d}{d\omega} = \frac{d\lambda}{d\omega}\frac{d}{d\lambda} = -\frac{\lambda^2}{2\pi c}\frac{d}{d\lambda}.$$

$$D = -\frac{2\pi c}{\lambda^2}\beta_2,$$

where: c is the speed of light in vacuum and λ is the operating wavelength. In practical terms, the chromatic dispersion parameter D relates to β_2 as:

$$\boxed{\beta_2 = -\frac{D\lambda^2}{2\pi c}.}$$

and thus:

$$\boxed{\Delta\tau_g = D\,\Delta\lambda\,z,}$$

which describes the temporal pulse over a propagation length z.

The third-order dispersion coefficient β_3 is defined as the derivative of β_2 with respect to angular frequency:

$$\beta_3 = \frac{d\beta_2}{d\omega}.$$

Substituting the derivative conversion between ω and λ:

$$\beta_3 = -\frac{\lambda^2}{2\pi c}\frac{d\beta_2}{d\lambda}.$$

Using $\beta_2 = -\dfrac{D\lambda^2}{2\pi c}$, we differentiate with respect to λ:

$$\frac{d\beta_2}{d\lambda} = -\frac{1}{2\pi c}\left(2\lambda D + \lambda^2\frac{dD}{d\lambda}\right).$$

Substituting this into the previous expression for β_3, we obtain:

$$\beta_3 = \frac{\lambda^2}{2\pi c}\cdot\frac{1}{2\pi c}\left(2\lambda D + \lambda^2\frac{dD}{d\lambda}\right) = \frac{\lambda^3 D}{(2\pi c)^2}\left(2 + \frac{\lambda}{D}\frac{dD}{d\lambda}\right).$$

remembering:

$$\beta_2 = -\frac{D\lambda^2}{2\pi c},$$

we differentiate β_2 with respect to λ using the product rule:

$$\frac{d\beta_2}{d\lambda} = -\frac{1}{2\pi c}\frac{d}{d\lambda}(D\lambda^2) = -\frac{1}{2\pi c}\left(\lambda^2\frac{dD}{d\lambda} + 2\lambda D\right).$$

Using the operator change

$$\frac{d}{d\omega} = -\frac{\lambda^2}{2\pi c}\frac{d}{d\lambda},$$

the third-order coefficient is

$$\beta_3 = \frac{d\beta_2}{d\omega} = -\frac{\lambda^2}{2\pi c}\,\frac{d\beta_2}{d\lambda}.$$

Substitute the expression for $d\beta_2/d\lambda$:

$$\beta_3 = -\frac{\lambda^2}{2\pi c}\left[-\frac{1}{2\pi c}\left(\lambda^2\frac{dD}{d\lambda} + 2\lambda D\right)\right] = \frac{\lambda^2}{(2\pi c)^2}\left(\lambda^2\frac{dD}{d\lambda} + 2\lambda D\right).$$

Collecting powers of λ yields the convenient forms

$$\boxed{\beta_3 = \frac{\lambda^3}{4\pi^2 c^2}\left(\lambda\frac{dD}{d\lambda} + 2D\right)}$$

or equivalently expanded:

$$\boxed{\beta_3 = \frac{\lambda^4}{4\pi^2 c^2}\frac{dD}{d\lambda} + \frac{\lambda^3 D}{2\pi^2 c^2}}$$

2.2 Kerr effect

The Kerr effect is the principal nonlinear phenomenon affecting optical field propagation in fibers. Physically, it manifests as a change in the refractive index of the fiber core. The refractive index variation is proportional to the instantaneous optical power and can be expressed as:

$$n(z,t) = n_L + n_2\frac{P(z,t)}{A_{\text{eff}}} \tag{2.6}$$

where n_L is the linear refractive index, n_2 is the nonlinear refractive index coefficient, and A_{eff} represents the effective mode area, i.e., the cross-sectional area where the optical power is confined within the fiber. By definition, the propagation constant β is related to the refractive index as:

$$\beta = \frac{2\pi}{\lambda}n \tag{2.7}$$

A change in the refractive index Δn therefore induces a corresponding change in the propagation constant:

$$\Delta\beta = \frac{2\pi}{\lambda}\frac{n_2}{A_{\text{eff}}}P(z,t) = \gamma P(z,t) \tag{2.8}$$

where the parameter

$$\gamma = \frac{2\pi n_2}{\lambda A_{\text{eff}}} \tag{2.9}$$

is defined as the nonlinear coefficient. The Kerr effect can thus be interpreted as an intensity-dependent modulation of the propagation constant β.

Considering the optical field $E(z,t)$, and neglecting higher-order terms, the evolution of the field envelope along the fiber is described by the nonlinear *Schrödinger equation (NLSE)*:

$$\frac{\partial E(z,t)}{\partial z} = -\alpha E(z,t) - j\frac{\beta_2}{2}\frac{\partial^2 E(z,t)}{\partial t^2} - j\gamma|E(z,t)|^2 E(z,t) \tag{2.10}$$

Here, the three terms respectively represent fiber attenuation, chromatic dispersion, and the nonlinear Kerr effect. The last term, $-j\gamma|E|^2E$, accounts for self-phase modulation (SPM).

Working in O-band and assuming zero dispersion ($\beta_2 \approx 0$), the NLSE simplifies to:

$$\frac{dE_n(z,t)}{dz} = -\alpha E_n(z,t) - j\gamma\left(2\sum_{m\neq n}|E_m(z,t)|^2 + |E_n(z,t)|^2\right)E_n(z,t) \tag{2.11}$$

The solution of this equation is:

$$E_n(z,t) = E_n(0,t)e^{-\alpha z}e^{j\phi_{\text{SPM}}}e^{j\phi_{\text{XPM}}} \tag{2.12}$$

where

$$\phi_{\text{SPM}} = -\gamma L_{\text{eff}}P_n(0,t) \tag{2.13}$$

$$\phi_{\text{XPM}} = -2\gamma L_{\text{eff}}\sum_{m\neq n}P_m(0,t) \tag{2.14}$$

and

$$L_{\text{eff}} = \frac{1-e^{-\alpha L}}{\alpha} \tag{2.15}$$

is the effective interaction length.

2.3 Cross-Phase Modulation (XPM)

Cross-phase modulation is a nonlinear process in which the intensity of one optical channel modulates the phase of another co-propagating channel through the Kerr effect. For two optical waves at frequencies ω_1 and ω_2:

$$E_{\text{total}}(z,t) = E_1(z,t) + E_2(z,t) \tag{2.16}$$

Each field can be expressed as:

$$E_i(z,t) = A_i(z,t)e^{j(\omega_i t - \beta_i z)} + c \tag{2.17}$$

For an N-channel WDM system, the total nonlinear phase shift affecting channel i is:

$$\phi_{\text{NL},i}(t) = \gamma L_{\text{eff}} \left[P_i(t) + 2\sum_{j\neq i} P_j(t) \right] \tag{2.18}$$

2.4 Four-Wave Mixing (FWM)

Four-wave mixing (FWM) is a third-order nonlinear optical effect resulting from the interaction of three optical waves that generate a new wave at frequency:

$$f_{mnk} = f_m + f_n - f_k \tag{2.19}$$

The generated FWM power is given by:

$$P_{mnk}(z) = D_2\gamma^2 P_m(0)P_n(0)P_k(0)e^{-2\alpha z} \left| \frac{1 - e^{-[2\alpha - j\Delta\beta_{mnk}]z}}{-2\alpha + j\Delta\beta_{mnk}} \right|^2 \tag{2.20}$$

where D_2 is the degeneracy factor and $\Delta\beta_{mnk}$ is the phase mismatch:

$$\Delta\beta_{mnk} = \beta(f_m) + \beta(f_n) - \beta(f_k) - \beta(f_{mnk}) \tag{2.21}$$

Expanding the propagation constant $\beta(f)$ around the zero-dispersion wavelength f_{ZDW}:

$$\beta(f) = 2\pi^2\beta_2(f - f_{\text{ZDW}})^2 + \frac{4}{3}\pi^3\beta_3(f - f_{\text{ZDW}})^3 \tag{2.22}$$

At the zero-dispersion wavelength ($\beta_2 = 0$), the phase mismatch is minimal, leading to efficient FWM generation. Conversely, in the C-band where $|\beta_2|$ is significant, the phase mismatch suppresses FWM efficiently.

The normalized FWM efficiency can be expressed as:

$$\eta_{\text{FWM}}(z) = D_2\gamma^2 e^{-2\alpha z} \frac{1 - 2e^{-2\alpha z}\cos(\Delta\beta z) + e^{-4\alpha z}}{4\alpha^2 + (\Delta\beta)^2} \tag{2.23}$$

In the case of $\Delta\beta = 0$:

$$\eta_{\mathrm{FWM}}(z) = D_2\gamma^2 e^{-2\alpha z}\frac{(1-e^{-2\alpha z})^2}{4\alpha^2} \tag{2.24}$$

This demonstrates why FWM efficiency is highest near the O-band, where chromatic dispersion vanishes ($\beta_2 \approx 0$), and strongly suppressed in the C-band, where dispersion breaks phase matching.

Chapter 3

Theory of Computational Performance in Fiber-Optic Simulation

The simulator used in this study models optical fiber propagation using the Split-Step Fourier Method (SSFM), a widely adopted numerical technique derived from the Nonlinear Schrödinger Equation (NLSE) [1, 10]. The SSFM approximates the evolution of the optical field by dividing the fiber into many small steps, Δz, and applying propagation in two separate parts: a linear part accounting for chromatic dispersion and attenuation, and a nonlinear part representing the Kerr effect, implemented through Fast Fourier Transform (FFT) and Inverse Fast Fourier Transform (IFFT) computations.

Because these operations are repeated for thousands of steps along the fiber, the computational workload becomes significant, particularly for high-resolution simulations, long fiber spans, or high launch powers. Understanding the runtime requirements of SSFM simulations is therefore critical for evaluating the performance of CPU- and GPU-based implementations, motivating the need to analyze and optimize both propagation and DSP processing times.

In particular the measurement of execution and propagation time in the fiber in IM-DD systems used for short distance data transmission is an important parameter to investigate.

3.1 Analyses of FFT transform times

Among all the computational processes involved, the most time-demanding functions are the *Fast Fourier Transform* (FFT) and its inverse (*Inverse Fast Fourier Transform*, IFFT), which are repeatedly executed during signal propagation in the *Split-Step Fourier Method* along the fiber SSFM.
Analyzing their execution time provides insights into the computational complexity of the simulator and helps identify opportunities for possible future optimization.

The analysis begins with the computation of the FFT applied to a randomly generated signal of length 2^k, where the transform is iterated 10^M times.
To measure the *average execution time* (in seconds) required to run a function, the `timeit` function is used. This built-in MATLAB function automatically executes the wanted function multiple times while mitigating warm-up effects such as JIT overhead. In MATLAB, the Just-In-Time (JIT) compiler introduces an initial overhead during the first execution of a function, as the code is compiled and optimized at runtime; `timeit` excludes this first execution and computes the average over the subsequent steady-state runs.

Moreover, the `timeit` function repeats each test until the total measurement duration exceeds a minimum threshold, which is typically around $0.1s$, ensuring reliability in the computed statistics. Then, it divides the total elapsed time by the number of iterations to obtain the average execution time per run.
In this analysis, the execution times of FFT were evaluated on vectors of length 2^k for $k = 10, 15, 30$, with the total number of repetitions $n = 10^M$ for $M = 2, 3, 4, 5, 6, 7$.

the *CPU* and *GPU* are two important components of a computing systems. The Central Processing Unit (CPU) serves as the main processing unit, designed for more general purpose tasks such as logic control and process management. It consists of a limited number of highly complex cores, each capable of running one or two threads that execute independent sequences of instructions in parallel.
The MATLAB command `maxNumCompThreads` was used to restrict the number of CPU threads employed in the FFT computations, allowing performance evaluation for the different numbers of active threads. In this study, the simulations were performed using $1, 3, 6$, and 12 CPU cores.

In contrast, the GPU (Graphics Processing Unit) is a massively parallel processor composed of thousands of simpler cores designed to execute identical operations concurrently across large datasets. It is characterized by high throughput and efficient parallel data processing capabilities. The GPU models used in this analysis were the *NVIDIA Tesla K40c* and *NVIDIA Tesla K80*.

The analysis presented in the following is based on the theoretical scaling relationship:

$$R = \frac{T(2^k)}{T(2^m)} = \frac{2^k \log_2(2^k)}{2^m \log_2(2^m)} \approx 2^{k-m} \cdot \frac{k}{m} \tag{3.1}$$

where $T(2^k)$ and $T(2^m)$ represent the average computation times for FFT operations of vectors of size 2^k and 2^m, respectively. This behavior derives from the theoretical computational complexity of the Fast Fourier Transform (FFT), which is $\mathcal{O}(N \log N)$.

For example, if we assume k=20 and m=10:

$$\text{Time}(2^{20}) = 2^{20} \times \log_2(2^{20}) = 2^{20} \times 20,$$

$$\text{Time}(2^{10}) = 2^{10} \times \log_2(2^{10}) = 2^{10} \times 10.$$

Thus, the expected theoretical ratio is:

$$\frac{\text{Time}(2^{20})}{\text{Time}(2^{10})} = \frac{(2^{20} \times 20)}{(2^{10} \times 10)} = 2^{10} \times 2 = 2048.$$

For the other cases analyzed in this thesis:

$$k = 15,\ m = 10 \quad \Rightarrow \quad \text{Theoretical ratio} = 48,$$

$$k = 20,\ m = 15 \quad \Rightarrow \quad \text{Theoretical ratio} \approx 42.67.$$

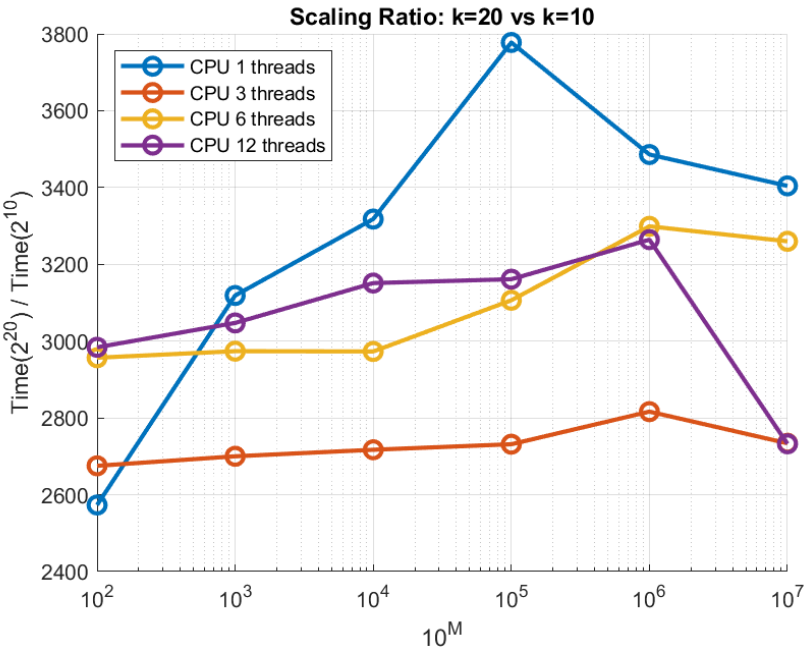

Figure 3.1: CPU simulation time of FFT assuming $k = 20$, $m = 10$

This figure 3.1 shows the ratio ranging from 2500 to 3800 for CPU configurations with $k = 20$ and $m = 10$, as a function of the number of CPU cores employed to evaluate the FFT. These results reflect memory overheads beyond the ideal $\mathcal{O}(N \log N)$ complexity. The single-thread CPU curve exhibits a peak around 10^5 repetitions with a ratio of approximately 3800, primarily due to cache effects and overhead. Initially, at 10^2 repetitions, performance is the better for the vector $2^(10)$, with a ratio of about 2600, which improves to around 3400 at 10^7,where the vector $2^(20)$ is computed much slower than the smaller vector $2^(10)$. This behavior illustrates the effects of the memory hierarchy, where system performance depends on the location of data within the storage structure. It ranges from fast and small units, such as registers and caches, to larger but slower units, such as main memory and disk.

At small data sizes, all data fit into the CPU cache that results in faster execution, while around 10^5 repetitions, the data remain in the cache where there is the peak of

the ratio that indicates a saturation of the memory bandwidth; moreover, at higher repetition counts, the cache can no longer accommodate all data, causing performance degradation due to frequent memory transfers to the main memory to complete the runs.

Multi thread configurations provide only limited gains showing minimal benefits from parallelization: even with 12 threads, the performance improvement remains modest, which is approximately 1.2, indicating poor thread scaling efficiency. At 10^7 repetitions with 12 threads, the performance becomes similar to the theoretical behavior due to parallel optimization of longer vectors. Anyway, in general at high repetition counts, performance efficiency drops because of memory bandwidth saturation and thread poor parallel synchronization. This behavior is consistent with *Amdahl Law*as described in [11], which describes the theoretical limit of the speedup achievable through parallelization:

$$S(N) = \frac{1}{(1-P) + \frac{P}{N}},$$

where:

- $S(N)$ is the total speedup with N threads;
- P represents the fraction that can be parallelized;
- $(1-P)$ represents the fraction that has to be serial.

As the number of threads increases, the maximum achievable speedup approaches $S(\infty) = \frac{1}{1-P}$. Therefore, the greater the parallelizable fraction of the code, the higher the potential speedup, though beyond a certain number of cores, adding more threads no longer improves performance and can even reduce it.

The implementations on GPU in the server (*NVIDIA Tesla K40c* and *NVIDIA Tesla K80*) demonstrate significantly better performance. This is shown in figures 3.2 3.3 and 3.4 achieving approximately 136 times faster execution than just one threaded CPU. Their scaling ratios remain nearly constant (less than 25 for ratio R of k=20 and m=10) across all repetition counts, demonstrating excellent parallel scalability. This indicates that for large vector sizes ($N = 2^{20}$), GPUs are fully utilized, whereas for small transforms ($N = 2^{10}$), they are underutilized and overhead effects can dominate.

For the figure 3.2, the $k = 15$ to $k = 10$ comparison, CPU implementations exhibit scaling ratios of approximately 35/45, close to the theoretical value of 48, indicating good algorithmic efficiency with these vectors' lengths.
In the figure 3.4, the$k = 20$ versus $k = 15$ comparison, CPU ratios increase to approximately 70/85 which is about twice the theoretical value of ~ 43 indicating that there are bottlenecks in the memory bandwidth, there are cache misses, therefore the latency hides the computational advantage. In contrast, GPU ratios remain stable at 15, much closer to the theoretical prediction. The memory bandwidth is higher than CPUs and relative overhead is much lower compared to the CPU case.

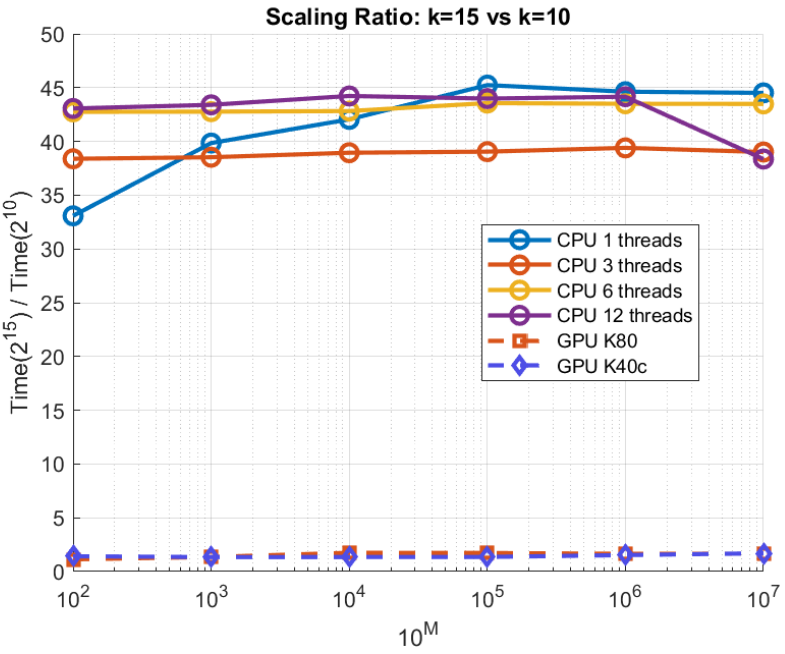

Figure 3.2: CPU vs GPU of the ratio R of the simulation times of FFT of $k = 15$, $m = 10$

Table 3.1 summarizes the performance metrics for FFT implementations and it reports the CPU architectures considered, the average execution time, the peak performance achieved, and the speedup relative to the baseline single-thread configuration at 10^7 repetitions. Efficiency is also included, showing how well the performance scales with the number of cores.

To evaluate CPU efficiency, we can define the following metric as:

$$\text{Thread Efficiency} = \frac{\text{Speedup}}{\text{Number of Threads}}.$$

As shown in Table 3.1, simulation results show that the most efficient configuration is with three threads, where Speedup = 1.2 and Efficiency = 40%, compared to six threads (Speedup = 1.0, Efficiency = 16%) and twelve threads (Speedup = 1.2, Efficiency = 10%) with respect to the single thread.

What can be observed is that higher number of threads do not necessarily lead to an increase in speedup or efficiency. It is clear that, besides using GPUs, for a large number of repetitions it is more effective to run 12 separate simulations with a single thread each in a CPU rather than one simulation using 12 threads.

Interestingly, the single thread and three thread configurations achieve slightly higher efficiency than the others in the analysis witk k=20 and m=10, possibly due to better

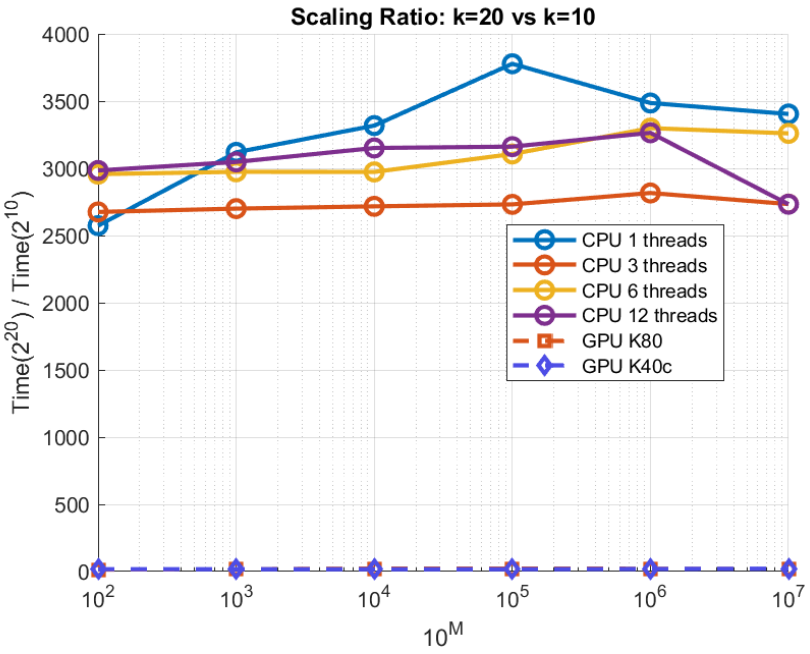

Figure 3.3: CPU vs GPU of the ratio R of the simulation times of FFT of $k = 20$, $m = 10$

Table 3.1: Performance Metrics Summary for FFT Implementations

Architecture	**Avg Time** $(2^{20}/2^{10})$	**Peak Performance @ M value**	**Speedup vs 1 Thread @10^7**	**Efficiency (%)**
1 Thread	3283	3800 @ 10^5	1.0×	100%
3 Threads	2767	2850 @ 10^6	1.2×	40%
6 Threads	3125	3300 @ 10^{6-7}	1.0×	16%
12 Threads	3092	3300 @ 10^6	1.2×	10%
GPU K40c	< 25	< 25	136×	—
GPU K80	< 25	< 25	136×	—

pipeline parallelism and cache utilization. Beyond six threads, performance gains diminish or even reverse, consistent with *Amdahl Law*. But it is clear that the single thread in CPUs is more instable during the performance for the different repetitions.

The CPU overhead growth and the cache's misses also confirm the memory bottleneck effect:

$$\text{Overhead Factor} = \begin{cases} \text{k=15/m=10:} & \sim 1.0 \text{ (ratio } \approx 45 \text{ vs. theoretical 48)}, \\ \text{k=20/m=15:} & \sim 2.0 \text{ (ratio } \approx 85 \text{ vs. theoretical 43)}, \\ \text{k=20/m=10:} & \sim 1.5 \text{ (ratio } \approx 3{,}300 \text{ vs. theoretical 2,048)}. \end{cases}$$

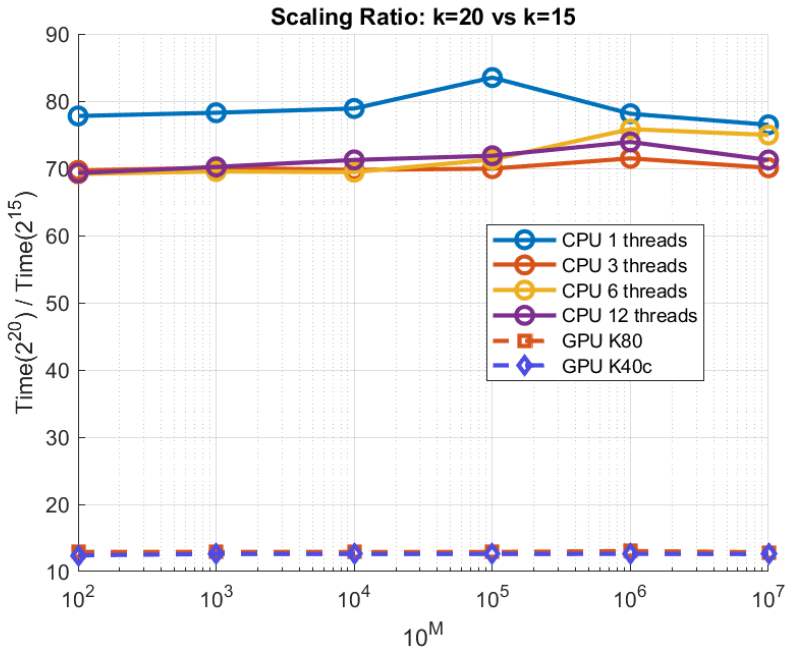

Figure 3.4: CPU vs GPU of the ratio R of the simulation times of FFT of $k = 20$, $m = 15$

The GPU performance curves in figure 3.5 show that both the *NVIDIA tesla K40c* and the*NVIDIA tesla K80* demonstrate excellent scaling behavior. The *NVIDIA tesla K80* exhibits a drastically worse performance near 10^4 repetitions, corresponding to optimal bandwidth occupancy, with a continued decline until 10^7 as the memory bandwidth becomes saturated. In contrast, the K40c displays an almost perfectly monotonic trend, consistent with its stable memory hierarchy and a worst performance at 10^7 repetition.

A quantitative comparison of scaling ratios for different FFT sizes is summarized in the following tab3.2:

Table 3.2: Experimental and theoretical scaling ratio for FFT Implementations

FFT Size Ratio	**Theoretical**	**CPU 1 Core**	**GPU**
$2^{15}/2^{10}$	48	35/45	2
$2^{20}/2^{15}$	42.7	70/85	15
$2^{20}/2^{10}$	2.048	2.500/3.800	25

These results confirm that GPUs are more efficient in executing the FFT algorithm, even overcoming the theoretical expectations.

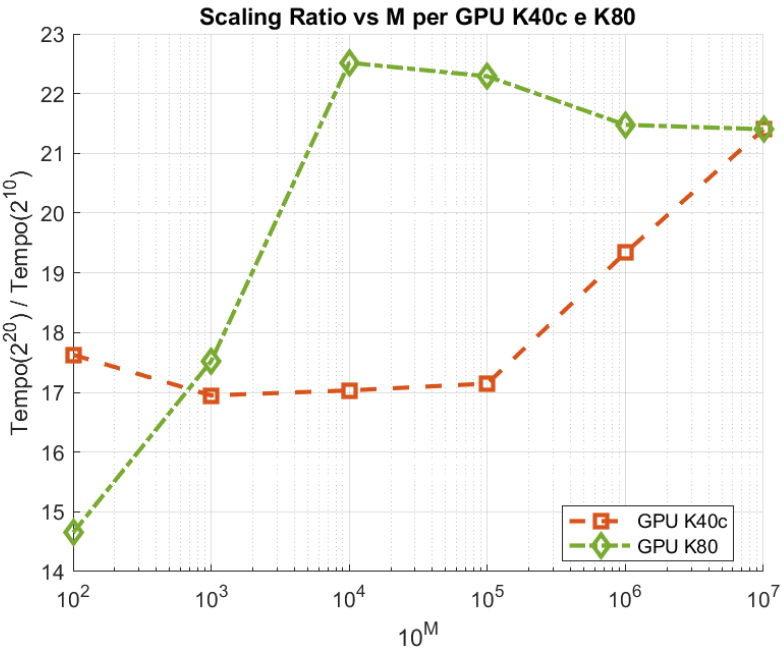

Figure 3.5: GPU simulation times of FFT with scaling factor $k = 20$, $m = 15$

In the end, the combined results demonstrate that GPU advantages grow with FFT size, as large transforms amortize launch overhead and fully utilize parallel resources. CPU threading yields limited benefits, with one and three threads emerging as the most efficient configuration before memory bandwidth saturation negates further gains. Overall, these observations confirm that for large FFT sizes ($k \geq 20$) and high repetition counts, GPUs clearly outperform CPUs, whereas for smaller vectors, GPUs are underutilized and CPU-based implementations can still achieve efficient performance.

Chapter 4

Simulation of Computational Performance in Fiber-Optic Simulation

Using the theory presented in the previous chapter, we emphasize the need to analyze the computational cost of our simulator, which models the SSFM based on the nonlinear Schrödinger equation.
By launching different channel powers, we calculated the simulation time, the DSP time, and especially the propagation time for the transmission of PAM4 with either 1 or 4 channels in an IM/DD system over the O-band.

Table 4.1 reports the computation times for the IMDD optical fiber transmission simulations under different launch powers ($P_{ch} = 0, 3, 6, 12$ dBm) for an PAM4 modulation over one channel. Three main stages are considered: signal propagation, simulation and digital signal processing (DSP).
The propagation stage, typically dominated by the split-step Fourier method with a tolerance step of $4e-4$ that changes the small steps, Δz, and shows that GPU acceleration provides a substantial computational advantage compared to CPU implementations. In particular, the *NVIDIA tesla K80* achieves propagation times between 2s and 15s, whereas a single-core CPU requires between 150s and 930s for the same task. Even with 12 cores, CPU times remain an order of magnitude higher because GPUs offer speedups in the range of $40-70$ times over one thread processing.
The total simulation time, reported in table 4.2, which includes the computational time of both split-step and DSP at the receiver side, follows a similar trend: the *NVIDIA tesla K80* and *NVIDIA tesla K40c* GPUs complete the task in approximately 45/55s, while CPUs go from 220/1000s depending on the number of cores. Parallel scaling on the CPU is evident but not linear, likely due to memory bandwidth and communication overheads.
The table 4.3 shows the DSP times, which remain relatively constant across different launch powers, but GPUs are approximately 1.5 times faster than CPUs; however, the difference between using GPUs and CPUs for the DSP process is not substantial, as they

change with the number of threads simulated. Table 4.1 reports the measured propagation time, comparing GPU and CPU performance across different channel power levels (P_{ch}). The results clearly show that GPU-based implementations are significantly faster than CPU-based ones, thanks to the parallel nature of the Split-Step Fourier Method (SSFM), which benefits from the high-throughput architecture of GPUs.

For example, at $P_{\text{ch}} = 0$ dBm, the GPU K80 completes the simulation in approximately 2.3 seconds, while the single-thread CPU requires nearly 150 seconds. Even with 12 CPU threads, the execution time remains around 69 seconds and still an order of magnitude slower than the GPU.

As P_{ch} increases, the propagation time grows for all architectures. This is due to the nonlinear effects becoming more pronounced at higher powers, which increases the computational complexity of the SSFM model. In particular, the number of required steps and the precision of the nonlinear phase calculation both contribute to longer times. The growth is especially steep for CPUs, which are less efficient at handling the parallelism required by SSFM under strong nonlinear conditions.

Table 4.1: Measured Propagation Time [s] in PAM4 modulation over one channel System Simulation

	GPU K40c	GPU K80	CPU–1	CPU–3	CPU–6	CPU–12
Pch = 0 dBm	2.7642	2.3234	149.5524	83.9198	78.3075	68.7779
Pch = 3 dBm	2.5343	2.2262	173.5888	101.2477	81.5830	75.2628
Pch = 6 dBm	4.0876	3.5297	308.2543	172.0962	138.5070	126.4397
Pch = 12 dBm	15.8392	13.9905	929.6855	353.1582	540.1103	251.7444

Table 4.2: Measured simulation Time [s] in PAM4 modulation over one channel System Simulation

	GPU K40c	GPU K80	CPU–1	CPU–3	CPU–6	CPU–12
Pch = 0 dBm	45.6072	48.7399	219.8596	164.3618	131.9482	128.0407
Pch = 3 dBm	44.2370	51.8283	244.5520	181.7799	132.0688	135.8639
Pch = 6 dBm	45.8284	52.0678	378.3116	241.5586	193.9587	180.6475
Pch = 12 dBm	57.2430	54.6668	999.0728	411.4209	593.0080	308.8712

Table 4.3: Measured DSP Time [s] in PAM4 modulation over one channel System Simulation

	GPU K40c	GPU K80	CPU–1	CPU–3	CPU–6	CPU–12
Pch = 0 dBm	42.8430	46.4165	70.3072	80.4420	53.6407	59.2688
Pch = 3 dBm	41.7027	49.6021	70.9632	80.5322	50.4588	50.5957
Pch = 6 dBm	41.7408	48.5381	70.0573	69.4624	55.4518	54.2078
Pch = 12 dBm	41.4038	40.6763	69.3873	68.2627	52.8977	57.1268

4.0.1 Computational Performance Analysis of PAM-4 over 4 Channels

The next analysis extends the study from single-channel PAM4 transmission to a four-channel PAM4 configuration. From a computational perspective, increasing the number of channels directly raises the simulation cost, since the SSFM model must process multiple signals in parallel while accounting for inter-channel nonlinearities. As a result, the propagation time grows compared to the single-channel case, reflecting both the higher data volume and the additional complexity introduced by cross-channel interactions.

The nonlinear step size is limited by the nonlinear phase rotation per step and changes as $\Delta z_{\text{nonlinear}} \propto 1/(\gamma P)$, where γ is the fiber nonlinear coefficient and P is the optical launch power. Higher launch power results in stronger Kerr nonlinearity, which reduces Δz and increases the number of steps. A power increase of 12 dB corresponds to a factor of $10^{12/10} \approx 16$, so the number of steps is proportional to the channel power and in this case can be deducted as:

$$N_{\text{steps}}(12\,\text{dBm}) \approx 16\, N_{\text{steps}}(0\,\text{dBm}).$$

However, the measured scaling shows only a ratio of 7/8 instead of the expected factor of 16, so number of steps does not scale perfectly linearly with power, and by fixed computational overheads that can become not predominant as the number of iterations increases.

As shown in the following tables 4.4 4.5 and 4.6 shows that PAM4 is more computationally demanding than the one over one channel simulation.

Table 4.4: Measured Propagation Time [s] in PAM4 System Simulation

	GPU K80	GPU K40c	CPU–1	CPU–3	CPU–6	CPU–12
Pch = 0 dBm	101.5020	86.0506	8060.8	5306.2	4627.8	4436.1
Pch = 3 dBm	505.0470	171.5477	15039	10374	8996.7	8568.4
Pch = 6 dBm	991.5687	341.3049	30098	20263	17825	17259
Pch = 12 dBm	1979.5	671.5669	59373	35917	35028	33925

Table 4.5: Measured simulation Time [s] in PAM4 System Simulation

	GPU K80	GPU K40c	CPU–1	CPU–3	CPU–6	CPU–12
Pch = 0 dBm	828.6768	398.7812	9317.2	6204.2	5393.8	5155.6
Pch = 3 dBm	1195.8232	488.2214	16292.8	11265.8	9752.2	9274.4
Pch = 6 dBm	1666.9	655.0443	31350	21161	18583	17965
Pch = 12 dBm	2466.1	988.6559	60630	40508	35781	34665

Increasing the launch power from 0 dBm to 12 dBm increases the propagation time, as it can be seen in Table 4.4, by a factor of 7/8 for both GPUs and CPUs. This growth is explained by the stronger nonlinear effects at higher powers, which force the SSFM model to use smaller step sizes and more iterations, thereby increasing the computational

Table 4.6: Measured DSP Time [s] in PAM4 System Simulation

	GPU K80	GPU K40c	CPU–1	CPU–3	CPU–6	CPU–12
Pch = 0 dBm	727.1748	312.7306	1256.4	898	766	719.5
Pch = 3 dBm	690.7762	316.6737	1253.8	891.8	755.5	706
Pch = 6 dBm	675.3313	313.7393	1252	898	758	706
Pch = 12 dBm	666.6	317.0890	1257	891	753	710

load. However, the GPU *NVIDIA Tesla K80* becomes 19.5× slower at high launch power compared to low power due to its lower memory bandwidth relative to the *NVIDIA Tesla K40c*, which causes it to saturate earlier.

Table 4.7: Measured Propagation GPUs Time [s] in PAM4 System Simulation

Power [dBm]	**K40c [s]**	**K80 [s]**	**K40 Advantage**
0	86.1	101.5	1.18
3	171.5	505.0	2.94
6	341.3	991.6	2.91
12	671.6	1979.5	2.95

In the 4.7 at high power, *NVIDIA tesla K40c* is nearly **three times faster** than the *NVIDIA tesla K80*. This inversion arises because the *NVIDIA tesla K40c* is more performing.

Table 4.8: Measured Propagation CPUs Time [s] in PAM4 System Simulation for $P_{\text{ch}} = 0\,\text{dBm}$

Threads	**Time [s]**	**Speedup respect 1 core**	**Efficiency**
1	8060.8	1.0	100%
3	5306.2	1.52	51%
6	4627.8	1.74	29%
12	4436.1	1.82	15%

Efficiency is calculated as: $\text{Efficiency} = \frac{\text{Speedup}}{\text{Threads}} \times 100\%$ and as the number of threads increases, efficiency typically decreases due to parallelization overhead.

Table 4.8 shows the split-step and DSP CPU/GPU times for PAM4 over four channels. The results indicate that using more than three threads does not improve performance, confirming strong memory bandwidth saturation. This trend persists across all power levels.

The *NVIDIA tesla K40c* is 90 times faster than just one thread CPU and it is even better than the FFT simulation were it was only 60 times faster. It is approximately 50 times faster versus 12 threads.

In this table 4.9 shows that for GPUs, the propagation time accounts for only 12/22% of total simulation time, while on CPUs it dominates 86/87%. The DSP calculation is

Table 4.9: Measured Split-step and DSP CPUs and GPUs Time [s] in PAM4 over 4 channels for $P_{\text{ch}} = 0\,\text{dBm}$

Configuration	**Propagation [s]**	**DSP [s]**
GPU K80	101.5 (12%)	727.2 (88%)
GPU K40c	86.1 (22%)	312.7 (78%)
CPU-1	8060.8 (87%)	1256.4 (13%)
CPU-12	4436.1 (86%)	719.5 (14%)

not as fast, indicating that these routines are not optimized by using GPU compared to CPU.

Table 4.10: Measured simulation CPUs and GPUs Time [s] in PAM4 over 4 channels for $P_{\text{ch}} = 0\,\text{dBm}$

Configuration	**Total Time [s]**	**Speedup vs CPU-1**
GPU K40c	398.7812	23.3
GPU K80	828.6768	11.2
CPU-12	5155.6	1.8
CPU-1	9317.2	1.0

Table 4.10 shows the total time and speedup versus the single-thread CPU for both GPUs and CPUs. It can be seen that the *NVIDIA Tesla K40c* is the most efficient technology for PAM4 simulation over four channels, achieving a total system speedup of 23.3 at $P_{\text{ch}} = 0\,\text{dBm}$ and maintaining consistent performance up to $P_{\text{ch}} = 12\,\text{dBm}$. The propagation process is 90× faster compared to the single-thread CPU, but it contributes only about 12% of the total runtime. The analysis also highlights that using 12 threads is only 1.8× faster than a single thread.
In conclusion, PAM4 workloads are found to be 30–50× more computationally demanding than single-channel transmission, reflecting the increased bit rate.

Chapter 5

Simulation Results

This chapter presents the numerical results obtained from the simulations, highlighting how both linear and nonlinear phenomena affect high-speed signal transmission in IM/DD systems operating in the O-band. The focus is placed on **PAM4 modulation**, which serves as the preferred format due to its spectral efficiency.

5.1 Chromatic dispersion and shift of the central frequency

Chromatic dispersion plays a critical role in determining the performance of PAM4 transmission, as it directly impacts signal integrity and the achievable bit error rate. This section investigates the dispersion effects and the shift of the central frequency, starting from the simplest case of single-channel transmission without added noise. The results provide insight into the sensitivity of the system to launch power and the onset of nonlinear distortion.

5.1.1 Analysis of Chromatic dispersion for PAM4 modulation over one channel

The analysis of the system begins with a simple simulation scenario, consisting of a single channel at zero-dispersion wavelength (1310 nm), trasmitting PAM4 modulation at 112GBd. For simplicity, no phase noise is added for modulating CW laser.

For different values of launched channel power, figure 5.1 shows the Bit Error Rate (BER) as a function of the Received Optical Power (ROP), evaluated across a wide range of channel launch powers ($P_{\text{ch}} = 0$ to 23 dBm). A horizontal dashed line at BER $= 3.8 \times 10^{-3}$ marks the hard-decision Forward Error Correction limit. By intersecting the BER vs ROP curves with this threshold, the required ROP at the target BER can be determined. The BER decreases as the received power increases, reaching a minimum at an optimal ROP before degrading again as the channel power increases. Around ROP $= -10$ dBm, a cascade in BER is observed, while beyond approximately 0 dBm the curves flatten for high launch powers ($P_{\text{ch}} > 20$ dBm).

At lower channel powers (0/9 dBm), the system achieves good performance (BER $\approx 10^{-4}/10^{-3}$), but for launch powers of (19/23 dBm), nonlinear impairments dominate, raising the BER floor up to 10^{-2} or higher and preventing operation below the FEC threshold.

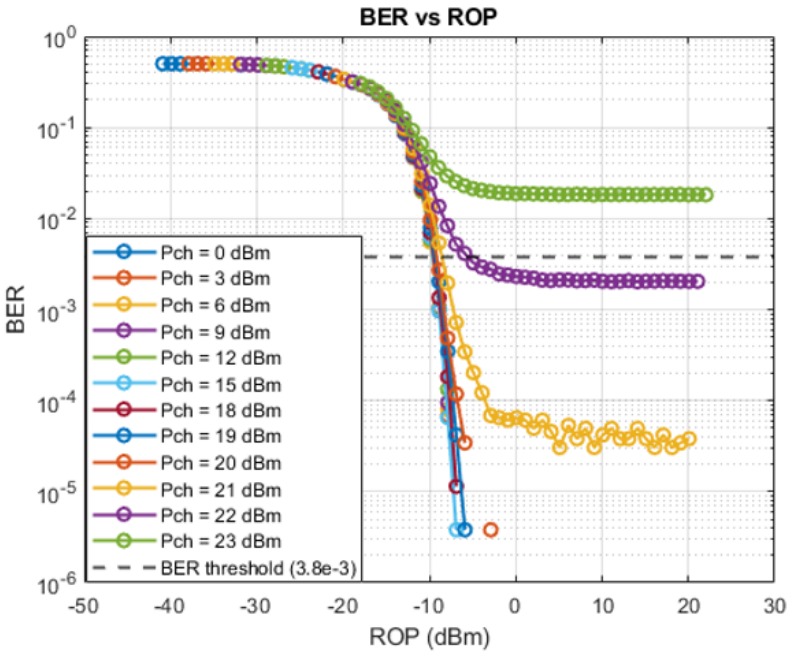

Figure 5.1: ROP vs BER for PAM4 modulation over one channel

A clearer analysis of ROP at BERt for different powers channels in figure 5.2, which illustrates that for launch powers below approximately 18 dBm, the required ROP remains nearly constant at about -9.5 dBm. A change occurs at $P_{\text{ch}} \approx 18$ dBm, closely corresponding to the theoretical nonlinear threshold $P_{\text{th}} \approx 1/(\gamma L_{\text{eff}})$, where $\gamma \approx 1.87$ W^{-1}km^{-1} and $L_{\text{eff}} = (1 - e^{-\alpha_{\text{lin}} L})/\alpha_{\text{lin}} \approx 7$ km, giving $P_{\text{th}} \approx 19$ dBm. Beyond this point, the required ROP increases exponentially with launch power, rising by nearly 4 dB as P_{ch} increases from 18 to 22 dBm. This behavior marks the onset of nonlinear effects, where maintaining the same BER requires higher received power. The optimal operating range lies between $P_{\text{ch}} = 15$ dBm and 18 dBm where it is possible to maximize power efficiency while avoiding nonlinear degradation.

The next step is to show ROP at BERt for different powers channels and nonlinear distortion begins to dominate around $P_{\text{ch}} \approx 6$ dBm as it is shown in 5.3 with phase noise equal to zero. The flat region corresponds to where the BER goes quickly to zero, whereas the rising portion reflects the region where nonlinear effects start to be dominant

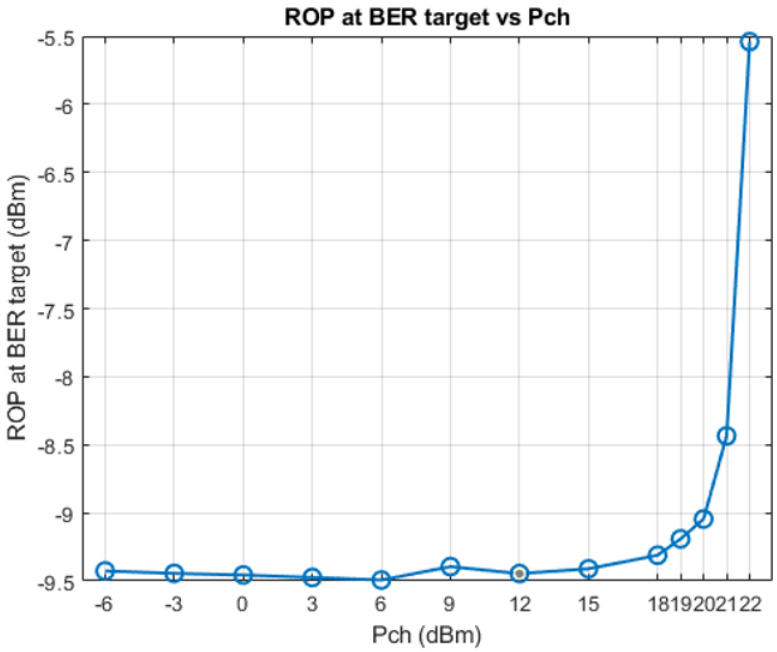

Figure 5.2: ROP at BER target vs P_{ch} for PAM4 modulation over one channel

for the signal.

For the PAM4 case over 4 channels, the linear operating region, where the required received optical power remains approximately constant at -9.5 dBm, extends only up to $P_{\text{ch}} = 6$ dBm. Beyond this point, the ROP rises sharply, reaching -6 dBm at $P_{\text{ch}} = 9$ dBm, corresponding to a 3.5 dB penalty for a 3 dB increase in launch power. This marks the onset of strong nonlinear distortion and contrasts with the single channel scenario in which the linear region exists up to $P_{\text{ch}} \approx 18$ dBm. The earlier nonlinear onset for PAM4, compared to PAM4 modulation over one channel configuration, that with more channels there are also XPM and FWM, not only SPM.

At $P_{\text{ch}} = 9$ dBm, nonlinear penalties of the channels become evident,indeed Channel 3 experiences a penalty of approximately 0.9 dB, Channel 4 about 2.3 dB, Channel 1 around 1.8 dB, while Channel 2 shows the strongest degradation (~ 3.3 dB).

As shown in the theory, as P_{ch} increases, the nonlinear phase shift

$$\phi_{\text{NL}} = \gamma P_{\text{ch}} L_{\text{eff}}$$

grows proportionally, inducing waveform distortion that requires higher ROP to maintain the same BER. The optimal operating point is therefore around $P_{\text{ch}} = 6$ dBm, maximizing transmission reach while avoiding nonlinear penalties.

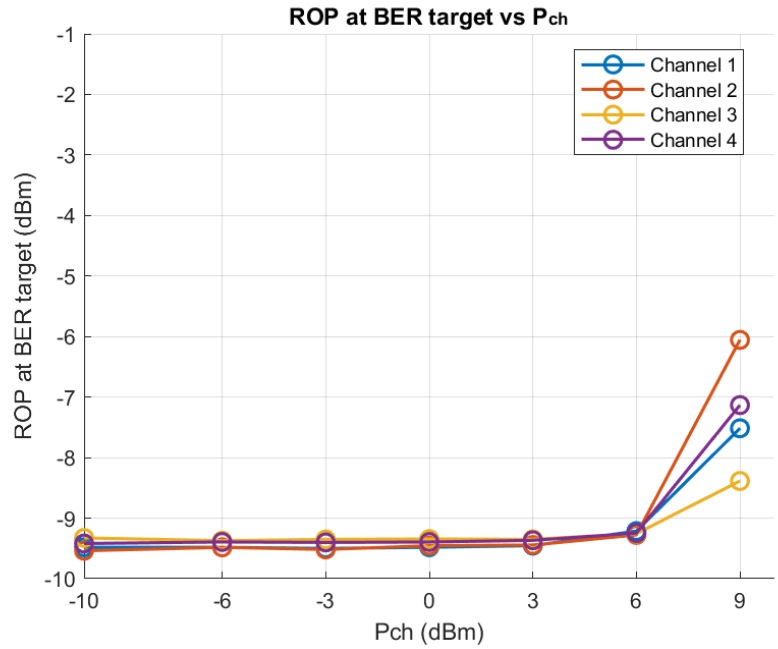

Figure 5.3: ROP at BER target vs Pch for PAM4 over 4 channels

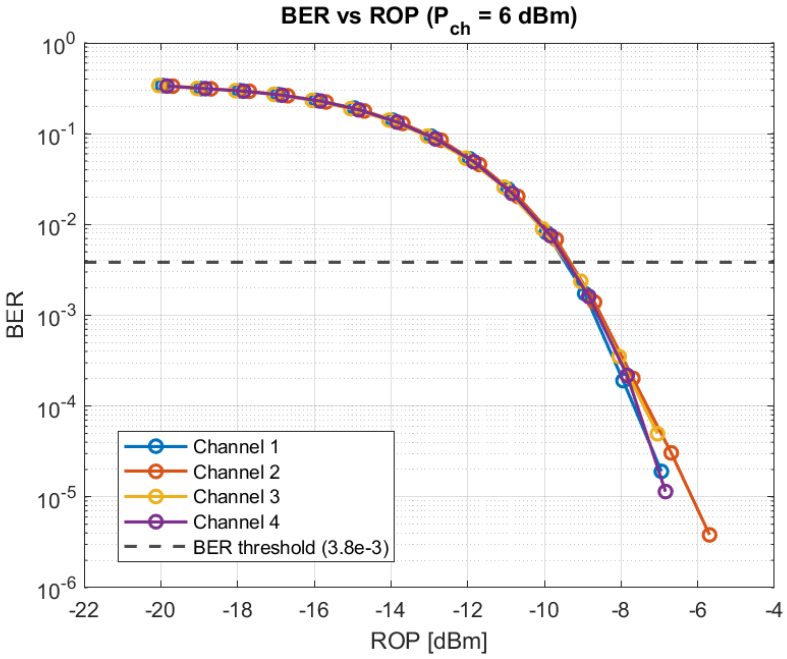

Figure 5.4: BER vs ROP for PAM4 over 4 channels

5.1.2 Analysis with frequency shift of the central frequency

Remembering that the goal of the project is to approach coherent like transmission performance with IM-DD system, the link must operate at high symbol rates, specifically 112 GBd, with a channel spacing of 400 GHz and a central wavelength of 1310 nm. This central wavelength lies between the central WDM channels. To fully characterize the behavior of the system, it is therefore necessary to investigate not only the central channel performance but also the edge channels where the effects of chromatic dispersion are not negligible.

For this reason, additional simulations are carried out by shifting the carrier frequency by $\Delta f = \pm 1, \pm 2, \pm 3$ THz, progressively moving away from the zero-dispersion condition typical of O-band transmission.

From theory, at the zero-dispersion frequency $f = f_{\text{ZD}}$ the dispersion coefficient is $D = 0$, corresponding to the minimum point of the dispersion function. Positive frequency offsets ($f > f_{\text{ZD}}$) lead to anomalous dispersion ($D > 0$), while negative frequency offsets ($f < f_{\text{ZD}}$) result in normal dispersion ($D < 0$).

This results in the typical parabolic shape with a minimum at $f = f_{ZD}$ and symmetrically increasing for larger $|\Delta f|$. The central channels (near f_{ZD}) show smaller penalties, while the lateral ones show increasing degradations.

Including both chromatic dispersion and four-wave mixing (FWM), the required received optical power can be expressed as:

$$\boxed{\text{ROP}_{\text{required}}(f) = \text{ROP}_0 + \text{Penalty}_{\text{dispersion}}(f) + \text{Penalty}_{\text{FWM}}(f)}$$

In practice, operating with a moderate offset from the zero dispersion wavelength reduces the FWM efficiency providing an optimal trade-off between noise, dispersion, and nonlinearity.

Figure 5.5 presents the co-polarized IM-DD transmission performance for frequency offsets of the central wavelength of $\Delta f = \pm 1, \pm 2, \pm 3$ THz and for various launch powers $P_{\text{ch}} = 0$, 3, 6, and 9 dBm. Removing the phase noise isolates the effects of chromatic dispersion and nonlinear effects, that become distinguishable.
At low launch powers, such as $P_{\text{ch}} = 0$ dBm, the system achieves the best overall ROP, since nonlinear effects are negligible. As the launch power increases, nonlinear penalties become dominant like for example at $P_{\text{ch}} = 9$ dBm, showing the strongest SPM and XPM contributions, combined with chromatic dispersion degradation and this nonlinear response demonstrates that higher power does not necessarily yield better performance. The plot also highlights that chromatic dispersion effects become more pronounced as the frequency offset increases. For small offsets ($f_{\text{shift}} = 1$ THz), the ROP remains nearly flat across all the channels, but at larger offsets ($f_{\text{shift}} = 2$ or 3 THz), the ROP increases progressively across the channel index, indicating stronger dispersion accumulation. In particular, for $f_{\text{shift}} = \pm 3$ THz, chromatic dispersion clearly dominates, with a difference of about +2 dB between Channel 1 and Channel 4.

At zero offset ($f_{\text{shift}} = 0$), chromatic dispersion is negligible at low power, as shown by the nearly flat ROP around −9 to −9.5 dBm. At higher power ($P_{\text{ch}} = 9$ dBm),

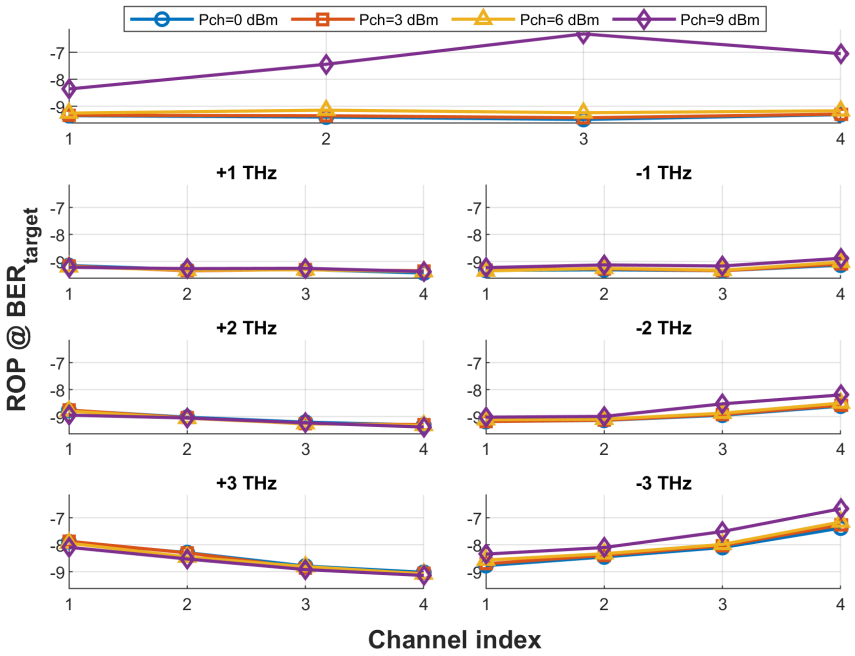

Figure 5.5: Effect of Frequency Offset on Chromatic Dispersion with $\phi_{\text{laser}} = 0$ kHz

nonlinear effects become clearly visible: the central channels experience the strongest degradation, confirming that FWM is the predominant impairment.

An asymmetry between positive and negative frequency offsets is also observed: the right-hand panels (negative offsets) show flatter ROP curves and smaller variations between power levels. This behavior is attributed to the dispersion slope D' and to the different signs of the interaction between dispersion and SPM and XPM, which may produce partial compensation on negative side of the spectrum.

From these observations, an optimal operating region emerges near $|f_{\text{shift}}| \approx 1$ THz, where dispersion penalties remain limited and nonlinear effects are still moderate.

5.1.3 Analysis of PAM4 adding phase noise

To further analyze the behavior of this transmission system, additional simulations were performed by introducing laser phase noise varying the laser linewidth.

Observing figure 5.6 the ROP at BER target versus P_{ch} with a phase-noise linewidth of 100 kHz and central frequency equal to 1310nm, we observe that until $P_{\text{ch}} \leq 0$ dBm, the system operates in the linear region, where all four channels exhibit nearly identical ROP requirements of approximately -9.3 dBm, remaining flat and uniform.

Starting from $P_{\text{ch}} = 1$ dBm, nonlinear effects begin to emerge, although they remain manageable. The optimal operating region lies between 1–3 dBm, where a favorable trade-off exists between received optical power, launch power, and nonlinear impairments. In this range, the system maintains good performance, with ROP values around

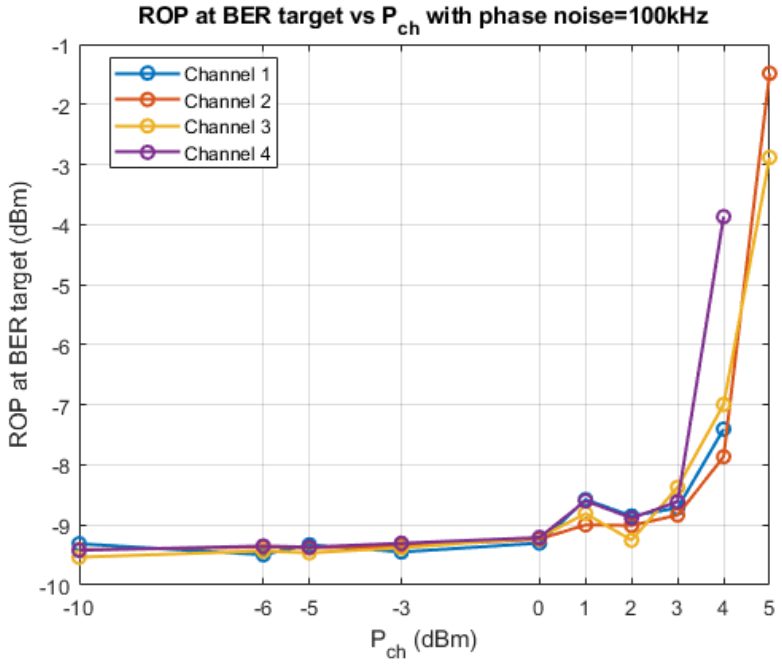

Figure 5.6: ROP at BER target vs P_{ch} with $\phi_{\text{laser}} = 100kHz$

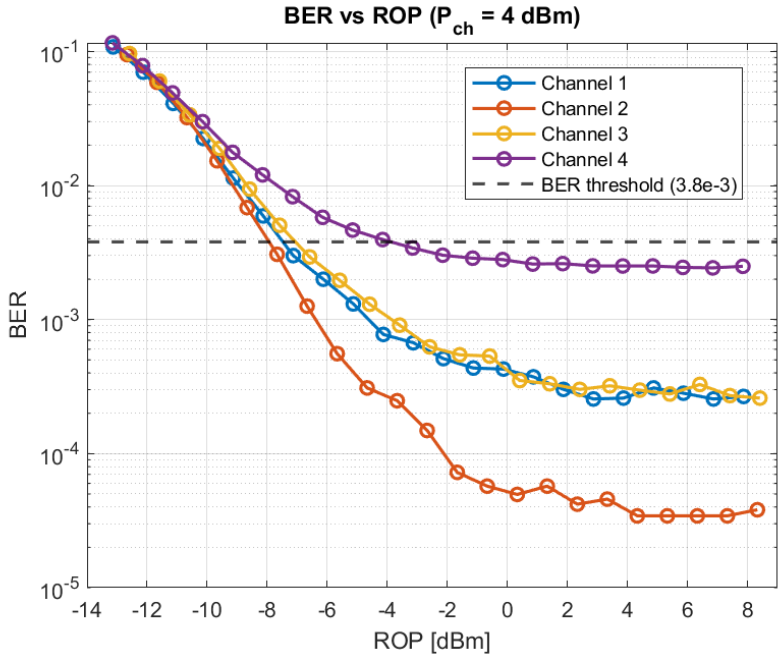

Figure 5.7: BER vs ROP with $P_{\text{ch}} = 4dBm$ and $\phi_{\text{laser}} = 100kHz$

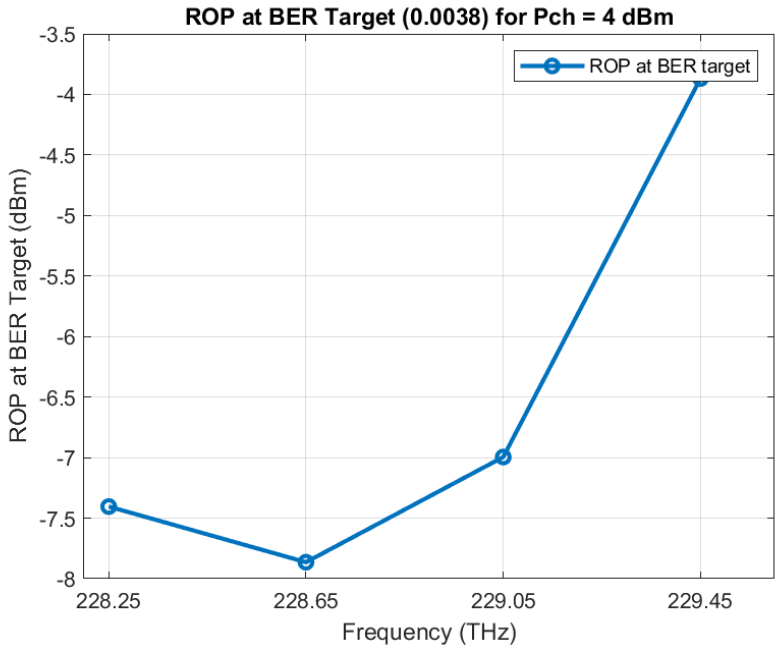

Figure 5.8: ROP at BER target vs channel frequencies with $P_{\text{ch}} = 4dBm$ and $\phi_{\text{laser}} = 100kHz$

-9 to -8.5 dBm. Beyond $P_{\text{ch}} = 3$ dBm, the system rapidly deteriorates due to strong nonlinear effects.

At $P_{\text{ch}} = 4$ dBm, as shown in figure 5.7, Channel 4 experiences the strongest degradation, requiring an additional 4.5 dB of ROP to achieve the same performance obtained at $P_{\text{ch}} = 3$ dBm.

Figure 5.8 reports the ROP required to reach the BER target of 3.8×10^{-3} as a function of optical frequency and unlike the case with an ideal laser, the linear operating region now ends at $P_{\text{ch}} \approx 4$–5 dBm instead of 9 dBm, due to the introduction of phase noise.

By $P_{\text{ch}} = 5$ dBm the signal degenerates irreparably, in particular Channel 2 requires a penalty of ~ 7.8 dB relative to the optimal region, while Channel 3 requires ROP ≈ -3 dBm and a ~ 6 dB penalty compared to the linear region. Channels 1 and 4 do not even reach the BER target at this power level, indicating that they are fully within the nonlinear region. The difference of the performance of edges and internal channels is due to the FWM as explained before.

These results demonstrate that, with a laser linewidth of 100 kHz, system performance begins to degrade at $P_{\text{ch}} \approx 3$ dBm, whereas in the ideal-laser case degradation started only beyond $P_{\text{ch}} = 6$ dBm. This confirms that phase noise significantly reduces the allowable launch power and strongly impacts overall system performance.

5.1.4 Analysis of the impact of different laser linewidth at Zero Dispersion

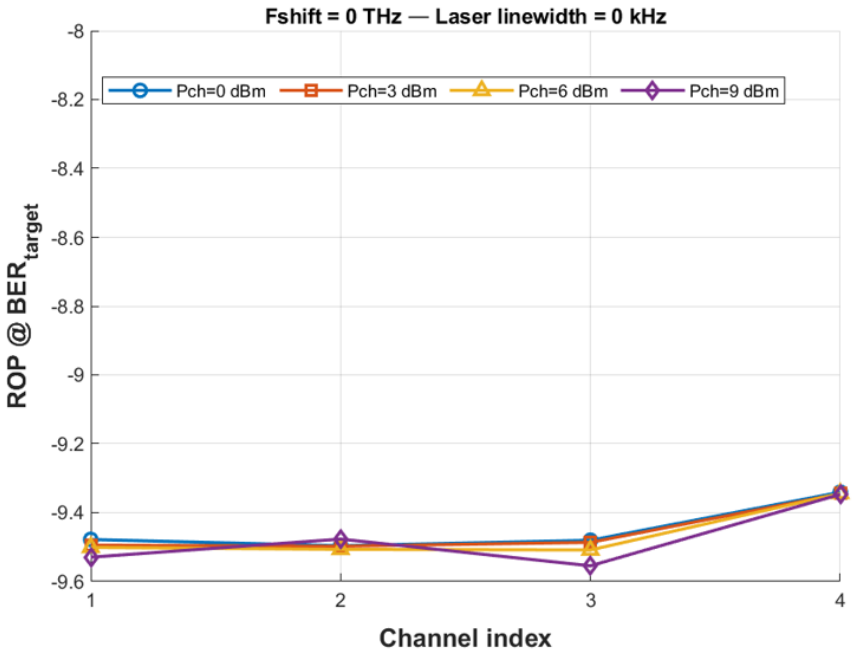

Figure 5.9: ROP at BER target vs channel frequencies with $\phi_{\text{laser}} = 0kHz$

The analysis is extended by evaluating the impact of different phase noise levels through several ROP per channel frequencies plots for various laser linewidths, shown in figures 5.9, 5.10, 5.11, and 5.12. The study, carried out at the zero-dispersion wavelength ($F_{\text{shift}} = 0$ THz), highlights the strong interplay between phase noise, nonlinear effects, and residual dispersion in PAM4 systems.

For the ideal case (laser linewidth = 0 kHz shown in figure 5.9), all power levels yield identical performance with ROP ≈ -9.5 dBm, confirming that nonlinear effects are negligible. When the linewidth increases to 10 kHz,figure 5.10, power dependent variations begin to appear at $P_{\text{ch}} = 6$ dBm, where the shaped channel response indicates dominant FWM effects at higher powers. For moderate linewidths (50 kHz),figure 5.11, nonlinear penalties become evident at $P_{\text{ch}} = 6$ and 9 dBm, as none of the channels reaches the BER target for any reasonable ROP value. At higher linewidths (100 kHz),figure 5.12, phase-noise penalties dominate: low powers ($P_{\text{ch}} = 0$ dBm) minimize degradation, while already at $P_{\text{ch}} = 3$ dBm the channels show noticeable impairment with ROP values around -8 dBm.

Across all linewidths, the central channel 3 consistently exhibits the best performance, whereas the edge channels suffer stronger degradation due to enhanced phase dispersion coupling. These results confirm that increasing the launch power does not necessarily improve system performance; rather, the optimal operating point depends

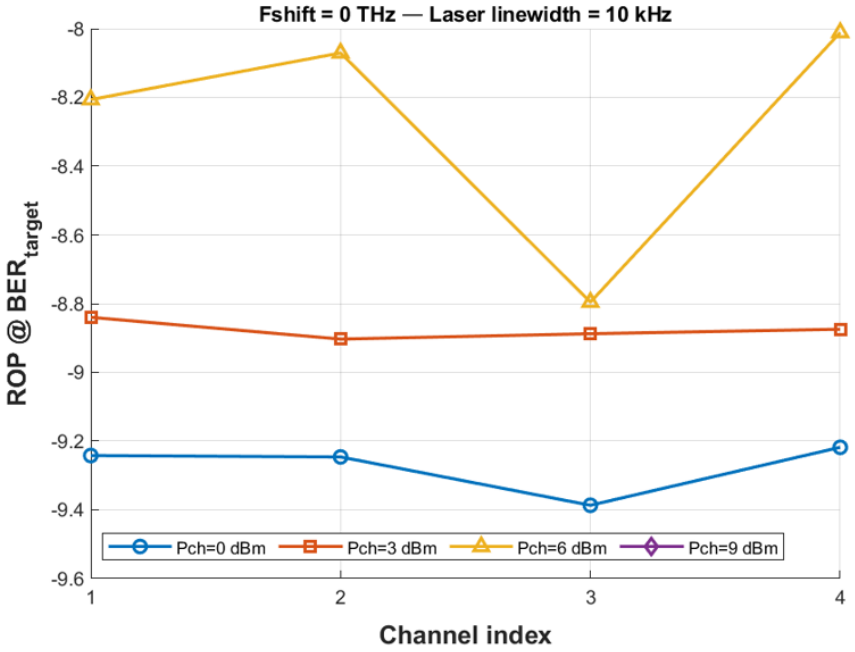

Figure 5.10: ROP at BER target vs channel frequencies with $\phi_{\text{laser}} = 10kHz$

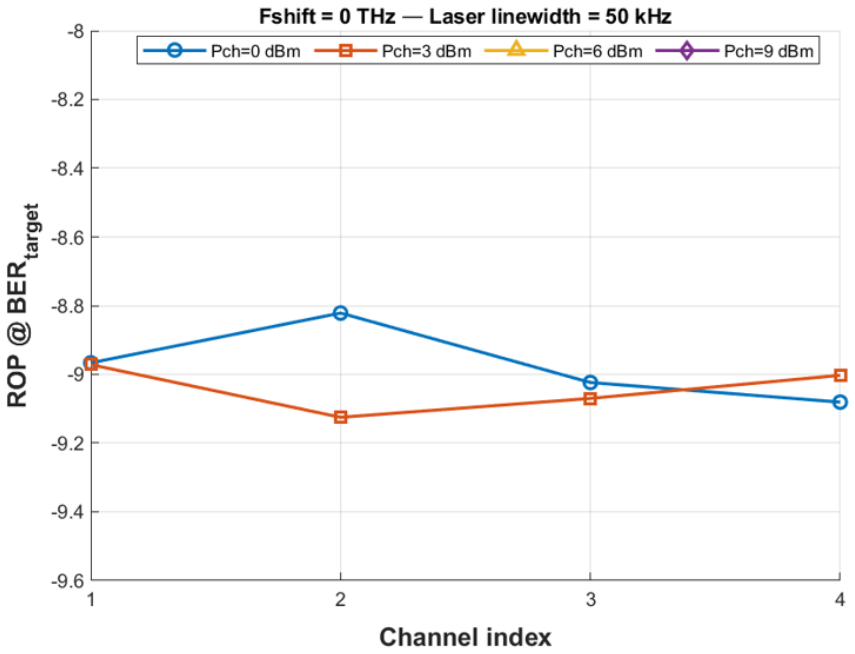

Figure 5.11: ROP at BER target vs channel frequencies with $\phi_{\text{laser}} = 50kHz$

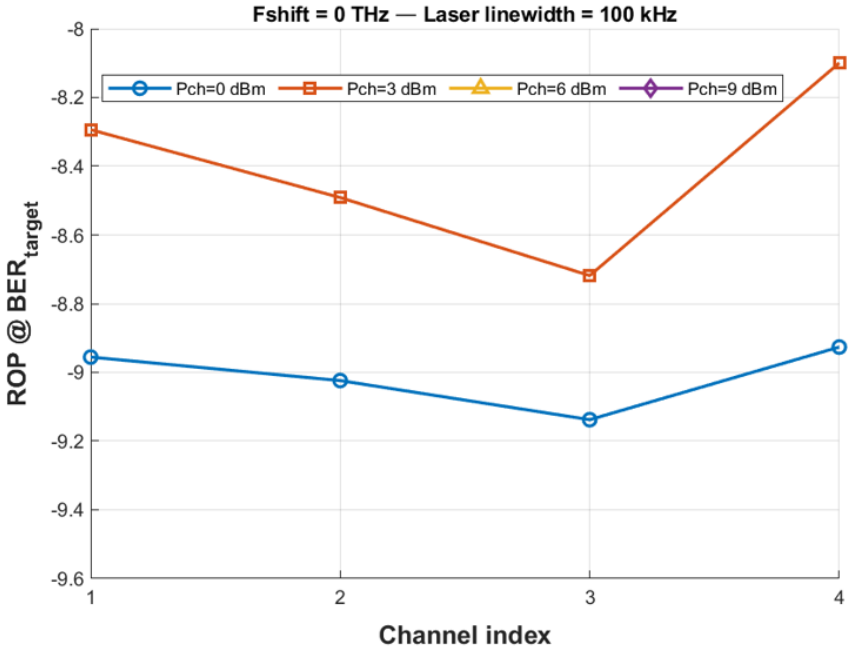

Figure 5.12: ROP at BER target vs channel frequencies with $\phi_{\text{laser}} = 100kHz$

critically on the laser linewidth. Laser with narrow linewidth ($\leq$ 10 kHz) perform best at low launch powers (0–3 dBm), moderate linewidths (around 50 kHz) achieve an acceptable balance, while broad linewidth sources ($\geq$ 100 kHz) require very low powers to mitigate nonlinear phase-noise penalties.

For a more in depth investigation, Figures 5.13 and 5.14 provide a clearer view of the system behaviour for laser linewidths of 10 kHz and 50 kHz, respectively.

For a laser linewidth of 10 kHz, it is evident that the linear operating region ends around $P_{\text{ch}} = 1$ dBm. Between $P_{\text{ch}} = 2$ and 4 dBm, phase noise effects become visible; however, the trade-off between the ROP required at the BER target and the launch power remains acceptable and the system still operates within a tolerable region. When increasing the power from $P_{\text{ch}} = 5$ to 7 dBm, the ROP required rises up to about ROP $= -6$ dBm, corresponding to a degradation of approximately 3.5 dB compared to the linear region.

For a laser linewidth of 50 kHz, the linear region extends up to $P_{\text{ch}} = 3$ dBm. A significant performance drop occurs at $P_{\text{ch}} = 4$ dBm, where the worst performing channel (Channel 2) requires ROP ≈ -6 dBm, corresponding again to a loss of about 3.5 dB when increasing the launch power by only 1 dB from $P_{\text{ch}} = 3$ to 4 dBm. This highlights the strong sensitivity of the system to phase noise at moderate linewidths particularly in combination with nonlinear propagation effects.

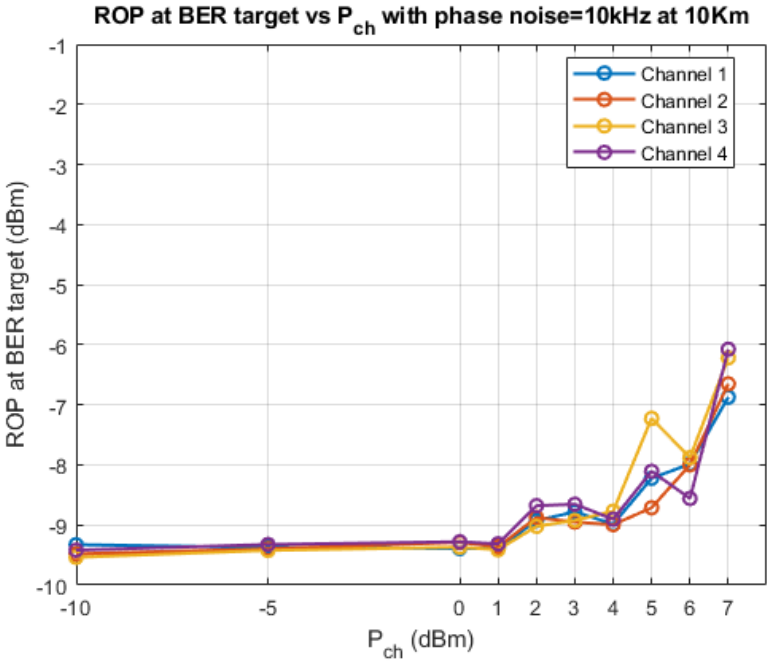

Figure 5.13: ROP at BER target vs P_{ch} with $\phi_{\text{laser}} = 10kHz$

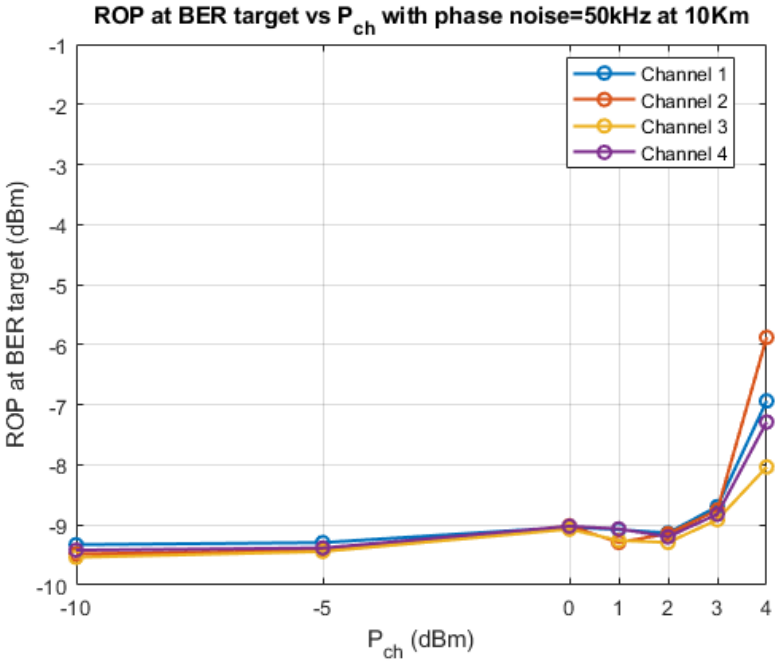

Figure 5.14: ROP at BER target vs P_{ch} with $\phi_{\text{laser}} = 50kHz$

5.1.5 Analysis with frequency shift of the central frequency adding $\phi_{\text{laser}} = 100kHz$

The figure 5.15 investigates the ROP at the BER target as a function of the channel frequencies for a laser linewidth of 100 kHz and for different frequency shifts of the central frequency. By shifting the central frequency for various launch powers ($P_{\text{ch}} = 0$, 3, 6, and 9 dBm), the figure illustrates how the visibility of chromatic dispersion and nonlinear effects changes relative to the phase noise introduced in the system.

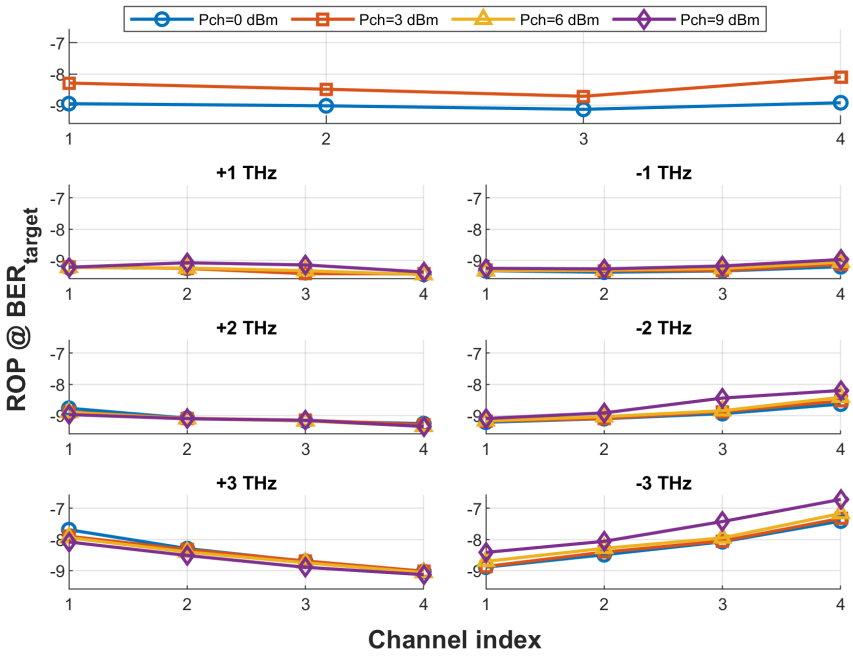

Figure 5.15: Effect of Frequency Offset on Chromatic Dispersion with $\phi_{\text{laser}} = 100kHz$

At low launch powers ($P_{\text{ch}} = 0$ dBm), the system achieves the best overall ROP performance, particularly at the central wavelength of 1310 nm. Indeed, as the power increases, nonlinear penalties rapidly dominate because the transmission operates exactly at the zero-dispersion point. In this condition, the degradation observed at $P_{\text{ch}} = 3$ dBm is solely due to phase noise, whereas for $P_{\text{ch}} = 6$ and 9 dBm, none of the channels' ROP reach the BER target.

The curves also show that chromatic dispersion effects increase as the optical frequency shifts away from the zero-dispersion point. For frequency offsets of ±1 THz, ±2 THz, and ±3 THz, a symmetric behaviour is observed: for negative offsets, Channel 1 exhibits the worst performance, whereas for positive offsets, Channel 4 becomes the most degraded. This confirms that when moving away from the central wavelength, chromatic dispersion becomes the dominant impairment, while phase-noise penalties tend to be mitigated by dispersion.

Operating exactly at the zero-dispersion wavelength reduces ISI and can enhance performance at high symbol rates; however, it also maximizes nonlinear interactions such as SPM and XPM and FWM. Under these conditions, phase noise produces the strongest degradation because its impact is not dispersed along the fiber and it is added to specially FWM effect. The system timing tolerance (TOL $= 4 \times 10^{-5}$) further highlights its sensitivity to non linear effects because they changes with time and reducing the step of the FFT along the propagation is more faithful to the analysis of FWM XPM and SPM.

5.1.6 Analysis for fiber length of 2 km

For completeness, we also analyse the system performance over a shorter transmission distance of 2 km, evaluating the impact of different laser linewidths (0, 10, 50, and 100 kHz).

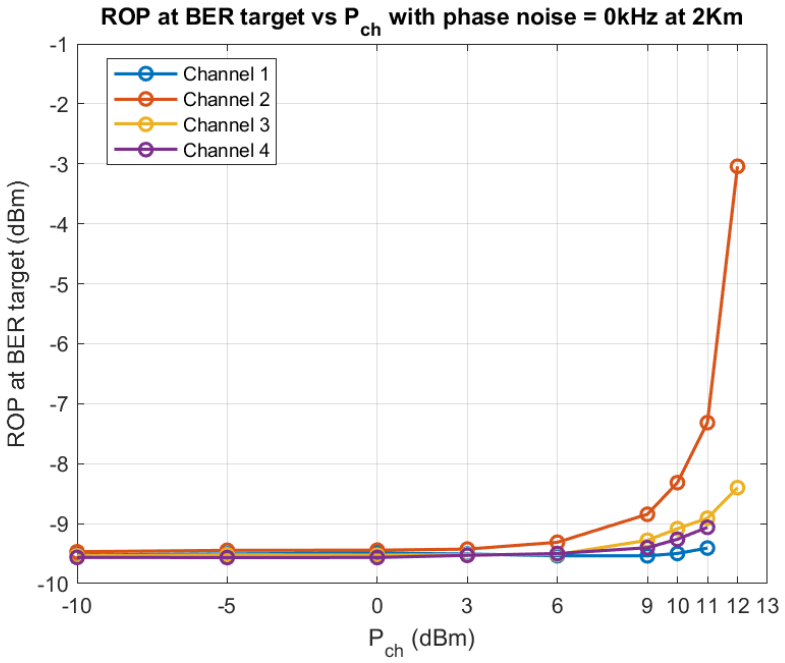

Figure 5.16: ROP at BER target vs P_{ch} with $\phi_{\text{laser}} = 0kHz$ and fiber length of 2km

From plots 5.16, 5.17, 5.18 and 5.19, it is clear that for short fiber reaches the signal begins to degrade at high channel powers. For a laser linewidth of 0 kHz (figure 5.16), the linear region extends up to approximately $P_{\text{ch}} = 10$ dBm, where the penalties are still acceptable and the required ROP remains below -8 dBm. At $P_{\text{ch}} = 12$ dBm, however, the signal begins to degrade significantly, especially for the edge channels.

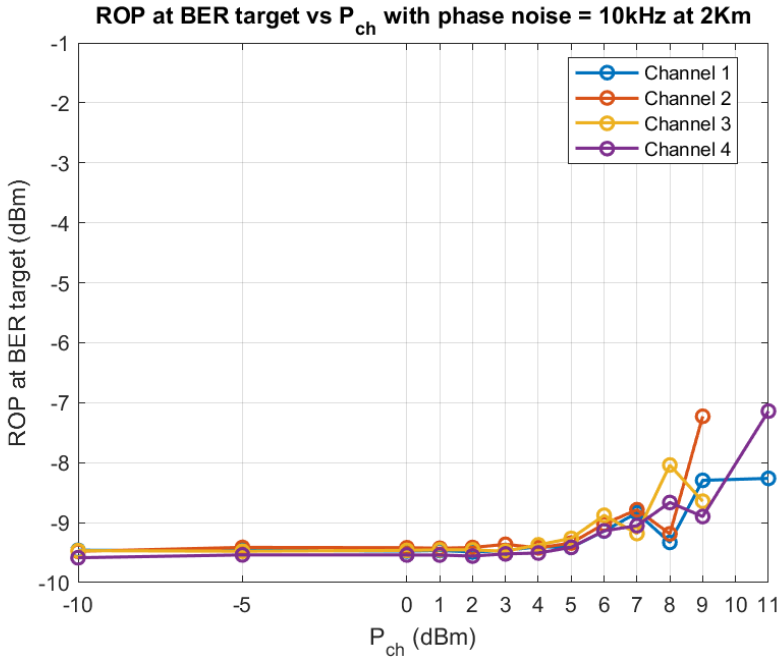

Figure 5.17: ROP at BER target vs P_{ch} with $\phi_{\text{laser}} = 10kHz$ and fiber length of 2km

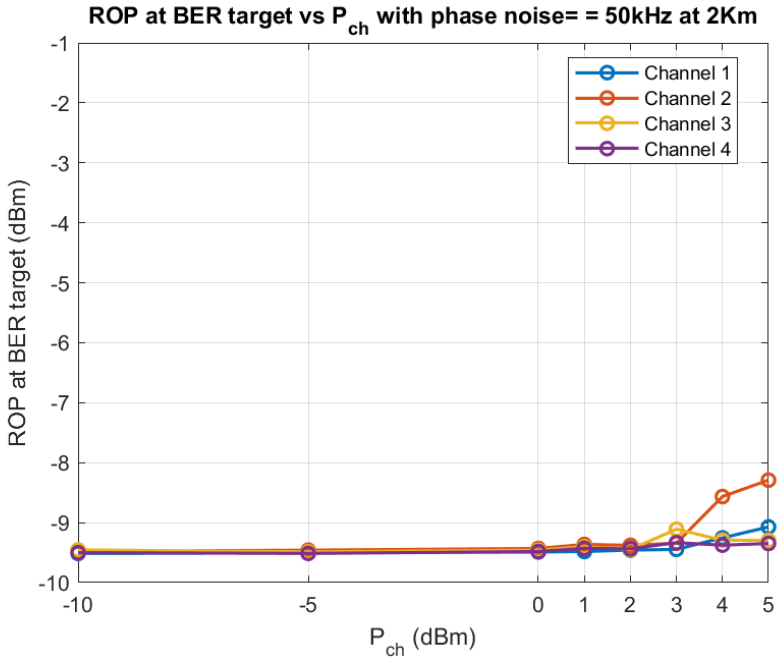

Figure 5.18: ROP at BER target vs P_{ch} with $\phi_{\text{laser}} = 50kHz$ and fiber length of 2km

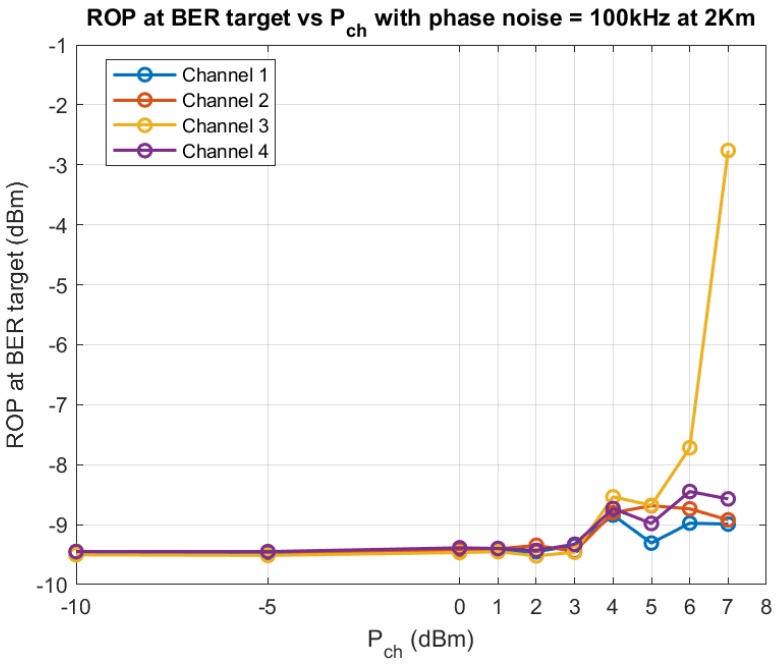

Figure 5.19: ROP at BER target vs P_{ch} with $\phi_{\text{laser}} = 100kHz$ and fiber length of 2km

For a linewidth of 10 kHz (figure 5.17), the optimal launch power is around $P_{\text{ch}} =$ 8 dBm, while noticeable degradation appears at about 9 dBm, and by 11 dBm only the outer channels remain within the acceptable ROP range which is an anomaly because at $P_{\text{ch}} = 10$ dBm all the channels do not reach the BER target and at 11 dBm that better channels should be the internal ones and not the edges channels.

For a linewidth of 50 kHz (figure 5.18), the linear operating region is reduced to approximately $P_{\text{ch}} = 5$ dBm. A similar behavior is observed for the 100 kHz linewidth case (figure 5.19), where the system also departs from the linear regime around 5 dBm and completely deteriorates at $P_{\text{ch}} = 7$ dBm, with the required ROP dropping to about -3 dBm, corresponding to a penalty of roughly 6.5 dB.

An important observation is that for both fiber lengths (2 km and 10 km), the optimal operating point in terms of the trade-off between P_{ch} and the ROP at the BER target is nearly identical for laser linewidths of 50 kHz and 100 kHz. This indicates that beyond a certain laser linewidth threshold, the additional phase noise does not significantly worsen system performance. Instead, most of the degradation occurs when increasing the linewidth from 0 to 50 kHz (with an intermediate transition at 10 kHz), while the difference between 50 kHz and 100 kHz becomes comparatively small.

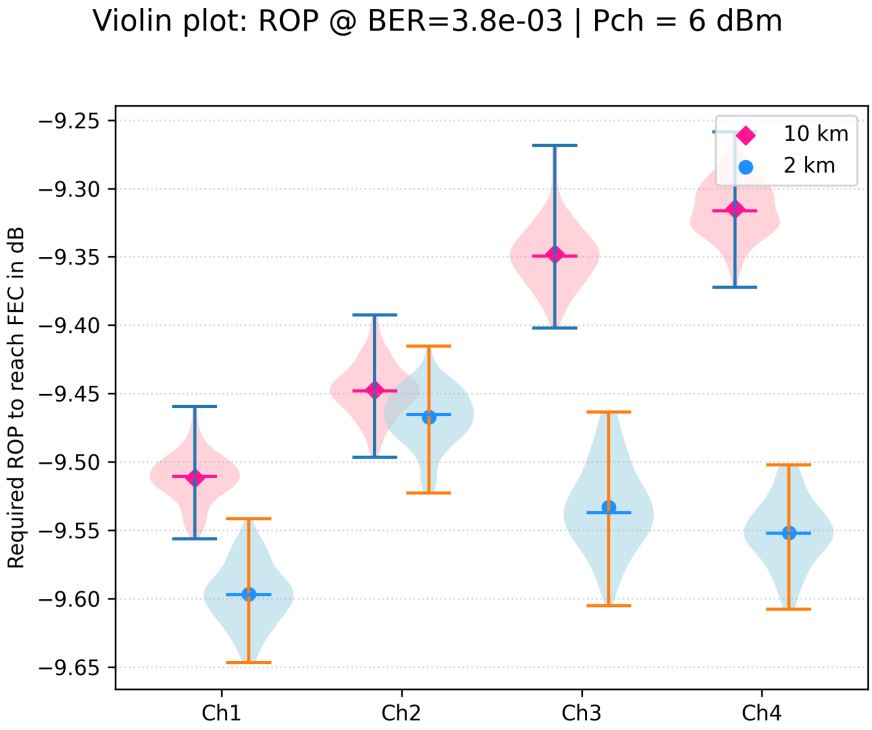

Figure 5.20: Distribution of Required ROP for co-polarization transmission with $P_{\text{ch}} = 6$ dBm and $\phi_{\text{laser}} = 0kHz$

5.1.7 Statistical performance analysis of the transmission with different laser noise and length fiber of 2km and 10km

For a very deep in analysis, the transmission is statistically evaluated over different fiber lengths and with different values of phase noise. To ensure a fair comparison, a fixed seed is used to always generate the same modulated signal,so that the same sequence of symbols was always transmitted, while a separate random seed controlled the noise in order to observe how the system performances change. A Monte Carlo procedure with 100 runs is implemented, and the corresponding ROP and BER results are saved and plotted.

These four plots 5.20, 5.23, 5.21 and 5.22 represent the statistical distribution of the ROP needed to achieve BER $= 3.8 \times 10^{-3}$ for the four channels for fiber lengths of 2km and 10km. The width of each violin represents the probability density and the central dot represents the mean, while the horizontal lines indicate the median and the quartiles. The four figures illustrate the optimal trade off between launch power and the required ROP to reach the FEC threshold for the co-polarization for different values of phase noise of the transmitting laser.

Figure 5.20, corresponding the trade off of non linear noises and launch power, which corresponds in this case at $P_{\text{ch}} = 6$ dBm, highlights that the chromatic dispersion is negligible at the zero dispersion wavelength. With this characteristics of the signal, there are still non linear effect especially the FWM that results in a characteristic degradation pattern across the four WDM channels in particular for the 10km length. In the absence of phase noise, however, the difference between the 2 km and 10 km transmissions remains limited: for 10 km, the ROP variation ranges approximately from -0.01 to -0.23 dBm, which remains below 1 dB across all channels. This confirms that, under ideal laser conditions, the impact of fiber length is comparatively small compared to the nonlinear penalties.

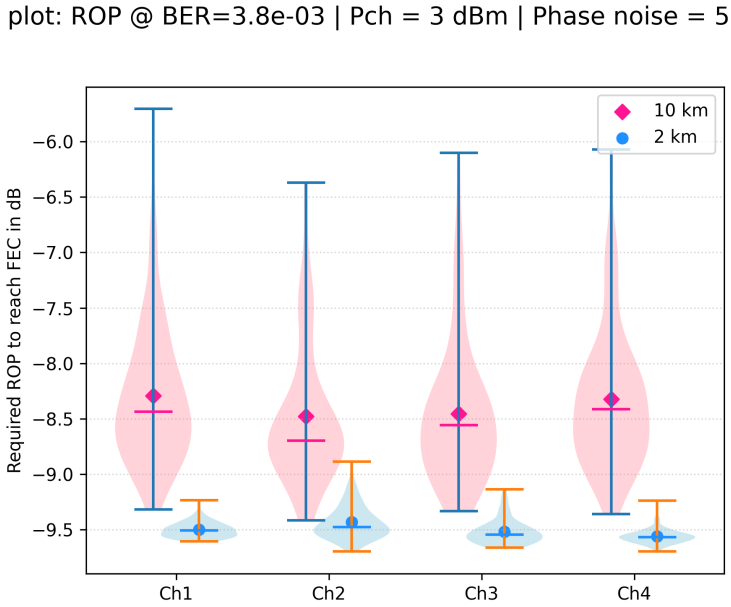

Figure 5.21: Distribution of Required ROP for co-polarization transmission with $P_{\text{ch}} = 3$ dBm and $\phi_{\text{laser}} = 50kHz$

At low launch powers, around $P_{\text{ch}} = 3$ dBm, the figures 5.21 and 5.22 show that the system operates in a very noisy signal. With this $P_{\text{ch}} = 3$ dBm, the crosstalk FWM remains weak and the impact of laser phase noise introduces only variability in the ROP.

For the 2 km link, increasing the linewidth does not significantly affect the transmission performance: the mean ROP across all channels remains close to -9.5 dBm, with no evident discrepancy between edge and central channels. In contrast, for 10 km the ROP required to reach the FEC threshold increases as the laser linewidth grows, but the penalty is relatively small, only 0.5 dB. The difference between the 2 km and 10 km links is approximately -1 dB for a 50 kHz linewidth and about -1.5 dB for a 100 kHz linewidth.

Moreover, increasing the phase noise from 50 kHz to 100 kHz noticeably broadens the

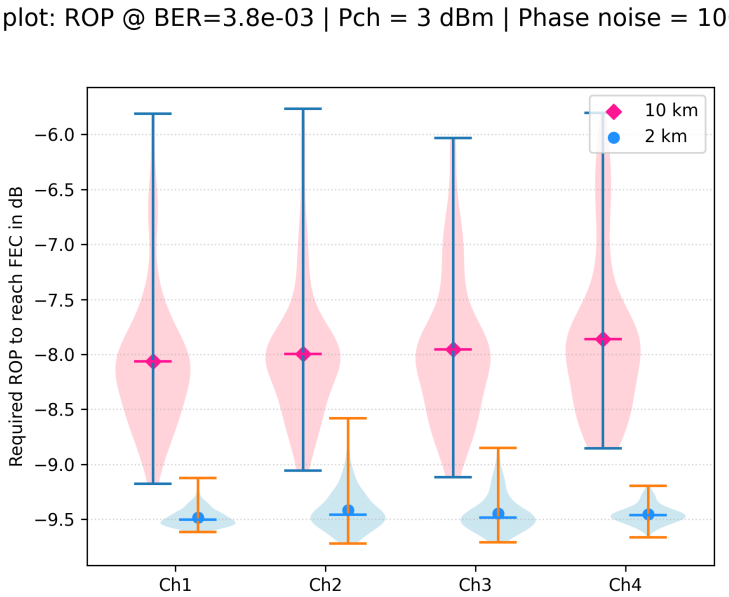

Figure 5.22: Distribution of Required ROP for co-polarization transmission with $P_{\text{ch}} = 3$ dBm and $\phi_{\text{laser}} = 100kHz$

ROP distribution, roughly doubling its spread. This behaviour indicates that phase fluctuations reduce signal stability, even though the mean ROP remains nearly unchanged, with differences on the order of only 0.5 dB.

At moderate launch powers ($P_{\text{ch}} = 4$ dBm) and low laser phase noise (10 kHz), as shown in figure 5.23, the system operates close to linear region. Under these conditions, channel responses remain highly uniform, FWM effects are still weak, and the overall transmission behaves almost deterministically. The difference in ROP between the 2 km and 10 km links (approximately 1–1.5 dB) is primarily attributable to fiber attenuation, while nonlinear accumulation remains limited at the considered channel power.

Although the nominal attenuation difference between 2 km and 10 km is

$$\alpha(10\text{ km}) - \alpha(2\text{ km}) = 0.35\text{ dB/km} \times 8\text{ km} = 2.8\text{ dB},$$

the measured ROP difference is only about 1.2 dB. This discrepancy is explained by the effective lengths:

$$L_{\text{eff}}(10\text{ km}) \approx 6.9\text{ km}, \qquad L_{\text{eff}}(2\text{ km}) \approx 1.95\text{ km},$$

The results further confirm that laser phase noise mainly increases the variability of the ROP rather than its mean level and the generated FWM power scales cubically with the launch power:

$$P_{\text{FWM}} \propto P_{\text{ch}}^3.$$

For stable system operation, laser linewidths below 50 kHz are recommended, since larger linewidths (> 100 kHz) introduce excessive fluctuations in the received power.

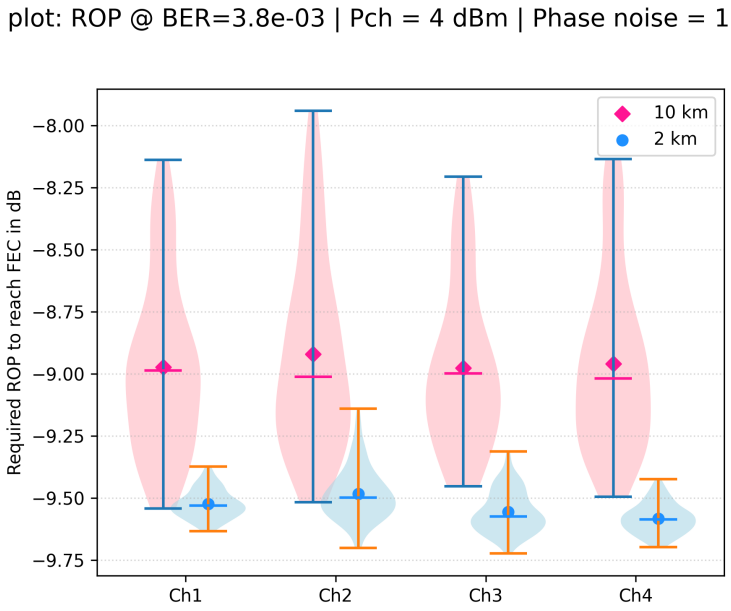

Figure 5.23: Distribution of Required ROP for co-polarization transmission with $P_{\text{ch}} = 4$ dBm and $\phi_{\text{laser}} = 10kHz$

For the 2 km transmission, the ROP distributions are extremely narrow and nearly vertical, showing spreads on the order of 0.1–0.2 dB. This behaviour indicates an almost deterministic system response, not dominated by the phase noise or FWM effect. In contrast, for 10 km, the violin plots exhibit significantly larger spreads (approximately 0.5/1.2 dB) and this broadening reflects the transition from a predominantly linear regime to a nonlinear and stochastic operating region.
In the end, phase noise accumulation increases linearly with the propagation distance, resulting in larger phase jitter and the interference between WDM channels becomes increasingly random. In addiction, also the nonlinear effects like are strongly amplified with distance. Since FWM depends on the relative phase relationships among interacting channels, phase noise transforms these interactions from coherent to partially incoherent, thereby increasing the statistical variability of the received signal.

The analysis is extended beyond the co-polarized configuration to include two additional polarization schemes, namely the **paired** and **alternating** configurations. These polarization have a significant impact on nonlinear interactions such as four-wave mixing (FWM) and cross-phase modulation (XPM).

- **Co-Polarization**: All channels share the same state of polarization and it represents the wost case scenario for nonlinear impairments as FWM and XPM that are maximized due to perfect polarization overlap.

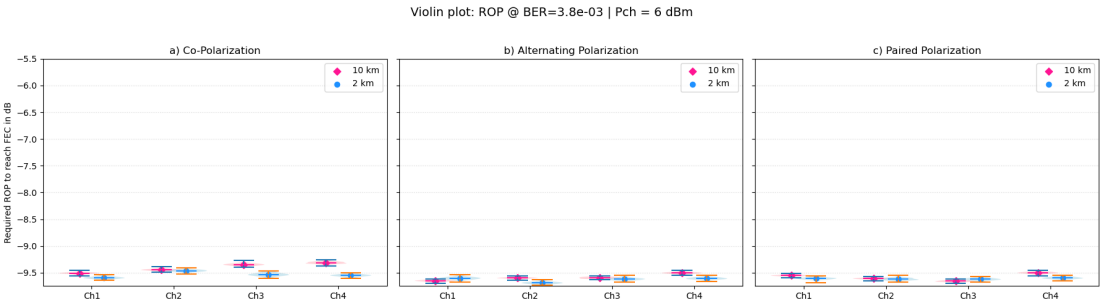

Figure 5.24: Distribution of Required ROP for all polarizations transmission with $P_{\text{ch}} = 6$ dBm and $\phi_{\text{laser}} = 0kHz$ for fiber lengths of 2km and 10km

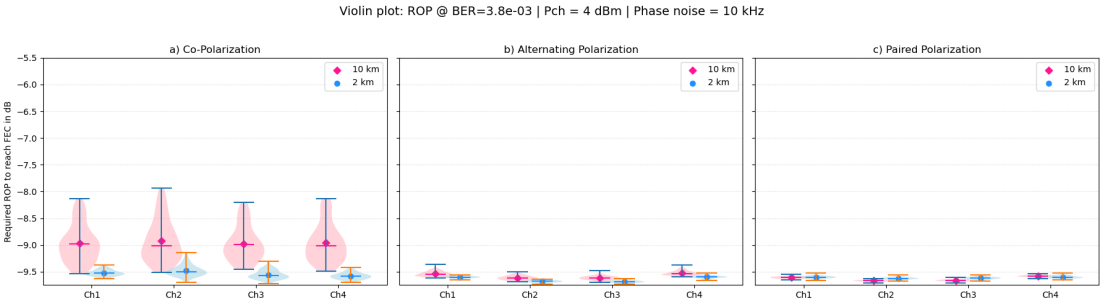

Figure 5.25: Distribution of Required ROP for all polarizations transmission with $P_{\text{ch}} = 4$ dBm and $\phi_{\text{laser}} = 10kHz$ for fiber lengths of 2km and 10km

- **Alternating Polarization**: Channels are arranged in an alternating pattern (X–Y–X–Y) and it reduces the impact of XPM and partially suppresses FWM efficiency, since adjacent channels are orthogonally polarized.
- **Paired Polarization**: Channels are grouped in pairs having the same polarization (X–X–Y–Y) and it results in intermediate nonlinear behavior and partially mitigated inter-channel coupling compared to co-polarization and alternating polarization.

In Figures 5.27 and 5.26, corresponding to $P_{\text{ch}} = 3$ dBm with laser phase noise of 100 kHz and 50 kHz respectively, the co-polarized configuration exhibits a clear difference between the 10 km and 2 km transmission distances as described before and in general the broader violin shapes indicate increased statistical variability driven by the laser phase noise. A clear distinction emerges between the co-polarized configuration and the paired/alternating schemes: for 10 kHz, 50 kHz and 100 kHz, the paired and alternating configurations maintain much lower ROP values and exhibit narrow, almost deterministic distributions for both 2 km and 10 km, indicating compensation for the non linear noise.

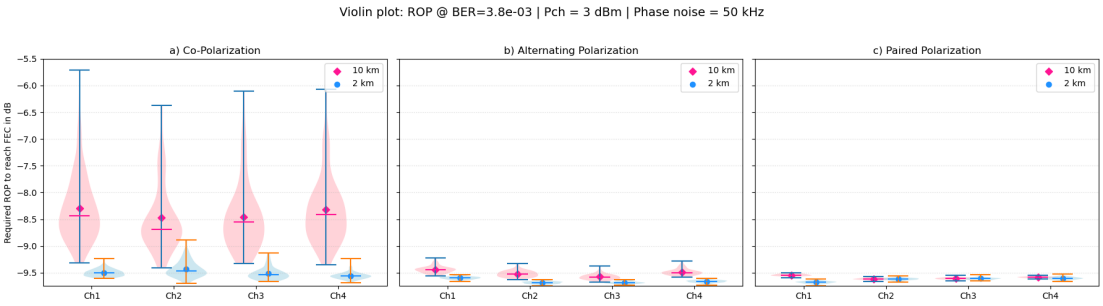

Figure 5.26: Distribution of Required ROP for all polarizations transmission with $P_{\text{ch}} = 3$ dBm and $\phi_{\text{laser}} = 50kHz$ for fiber lengths of 2km and 10km

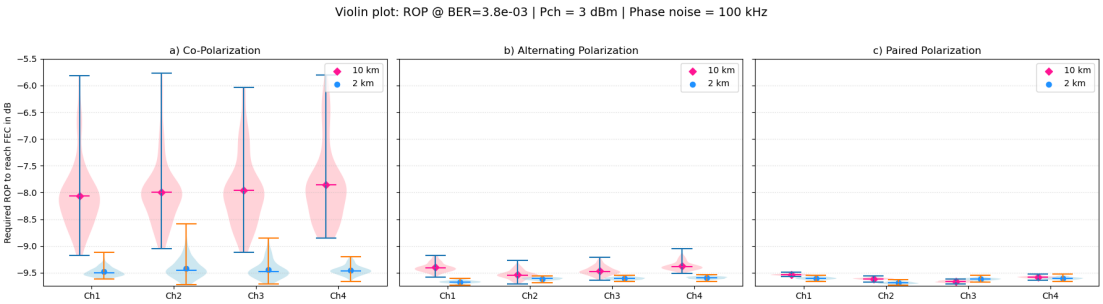

Figure 5.27: Distribution of Required ROP for all polarizations transmission with $P_{\text{ch}} = 3$ dBm and $\phi_{\text{laser}} = 100kHz$ for fiber lengths of 2km and 10km

In Fig. 5.24, with $P_{\text{ch}} = 6$ dBm and zero phase noise ($\Delta\nu_{\text{laser}} = 0$ kHz), the co-polarized configuration shows only subtle differences among the channels especially for 10km length fiber:

$$\text{Ch1} \approx -9.52 \text{ dBm}, \quad \text{Ch2} \approx -9.44 \text{ dBm}, \quad \text{Ch3} \approx -9.36 \text{ dBm}, \quad \text{Ch4} \approx -9.35 \text{ dBm}.$$

Since four-wave mixing scales as $P_{\text{FWM}} \propto P_{\text{ch}}^3$, doubling the launch power results in an eight times FWM increase, which explains the slightly stronger degradation observed on the edge channels compared to the central ones.

The alternating and paired polarization configurations remain highly effective, introducing only minimal asymmetries (on the order of 0.1 dB) between the channels. For both 2 km and 10 km fiber lengths, the three polarization schemes show nearly identical performance: the difference between edge and central channels is negligible, and the mean ROP varies by no more than 0.2 dB across polarization configurations.

The violin plots exhibit a very narrow statistical spread, indicating that the transmission remains highly deterministic despite the presence of nonlinear effects.

The violin plots, figures 5.28 and 5.29 illustrate the required Received Optical Power (ROP) to reach the Forward Error Correction (FEC) threshold at a Bit Error Rate (BER) of 3.8×10^{-3}, under a frequency shift of -3 THz. This spectral offset introduces

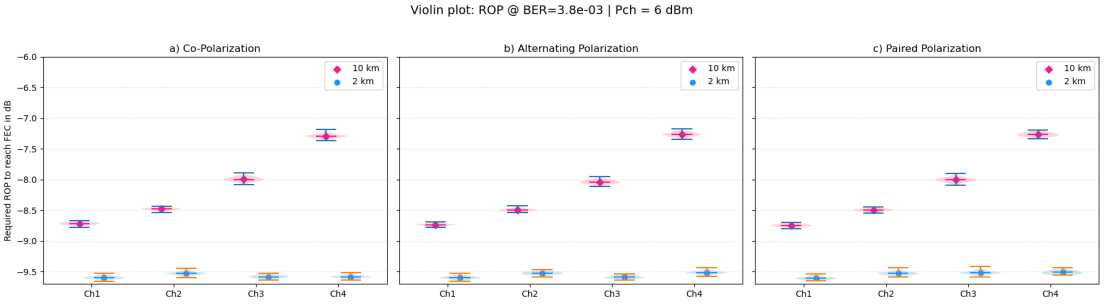

Figure 5.28: Distribution of Required ROP for all polarizations transmission with $P_{\text{ch}} = 6$ dBm and $\phi_{\text{laser}} = 0kHz$ for fiber lengths of 2km and 10km with Frequency Shift of -3 Thz

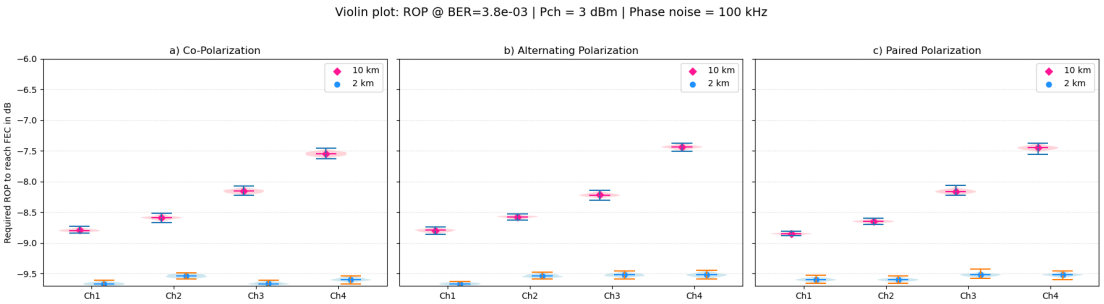

Figure 5.29: Distribution of Required ROP for all polarizations transmission with $P_{\text{ch}} = 3$ dBm and $\phi_{\text{laser}} = 100kHz$ for fiber lengths of 2km and 10km with Frequency Shift of -3 Thz

significant chromatic dispersion (CD), which increase with transmission distance. As shown in both figures, the ROP distributions for 10 km are consistently higher than those for 2 km, confirming that CD-induced waveform distortion accumulates with propagation length.

Despite the use of different polarization configurations, Co-Polarized, Alternating, and Paired, no substantial performance improvement is observed. This is because polarization diversity primarily mitigates nonlinear impairments, while chromatic dispersion remains unaffected by polarization state. Therefore, under strong CD conditions caused by the frequency shift, the system performance is dominated by linear dispersion effects rather than nonlinearities and polarization strategies offer limited benefit.

Chapter 6

Simulation Test

The investigation of chromatic dispersion (CD) is fundamental in this thesis, since, as previously shown,it introduces inter symbol interference (ISI), leading to signal distortion. The 4-PAM modulation format and its performance are particularly sensitive to the channel spacing, making the transmission more vulnerable to chromatic dispersion related impairments.

A widely adopted solution for compensating the dispersion in the C-band is the dispersion compensating fiber (DCF). A DCF is a specially engineered optical fiber that has negative dispersion, typically in the range of -80 to -100 ps/(nm $\cdot$ km) around 1550 nm wavelength, instead standard single-mode fiber (SMF) presents positive dispersion of approximately +16 to +18 ps/(nm $\cdot$ km). In contrast, dispersion parameter is 0 ps/(nm $\cdot$ km) in the O-band. In this simulation test, DCF is inserted in an optical link to counteract the accumulated remaining dispersion introduced during transmission through SMF and to isolate nonlinear effects. The main advantage of using DCF is its ability to effectively compensate chromatic dispersion, leading to improved signal quality and reduced BER.

In the present system, the combination of wide channel bandwidths shifts part of the signal spectrum away from the zero-dispersion point. For this reason, the main idea is to insert an ideal DCF implemented in the project with the same length of the SMF, using the MATLAB fiber object, designed such that

$$\beta_{2,\mathrm{DCF}} = -\beta_{2,\mathrm{SMF}}, \qquad \beta_{3,\mathrm{DCF}} = -\beta_{3,\mathrm{SMF}},$$

thus providing the negative dispersion necessary to compensate for the residual dispersion accumulated in the link. Non-linear coefficent (1/(W m) should be zero.

6.0.1 Simulation Test Results

The simulation is evaluated for different launch powers of the channels, in particular for -10 dBm -5 dBm 0 dBm 3 dBm 5 dBm with $\phi_{\mathrm{laser}} = 0kHz$ and $\phi_{\mathrm{laser}} = 100kHz$ and

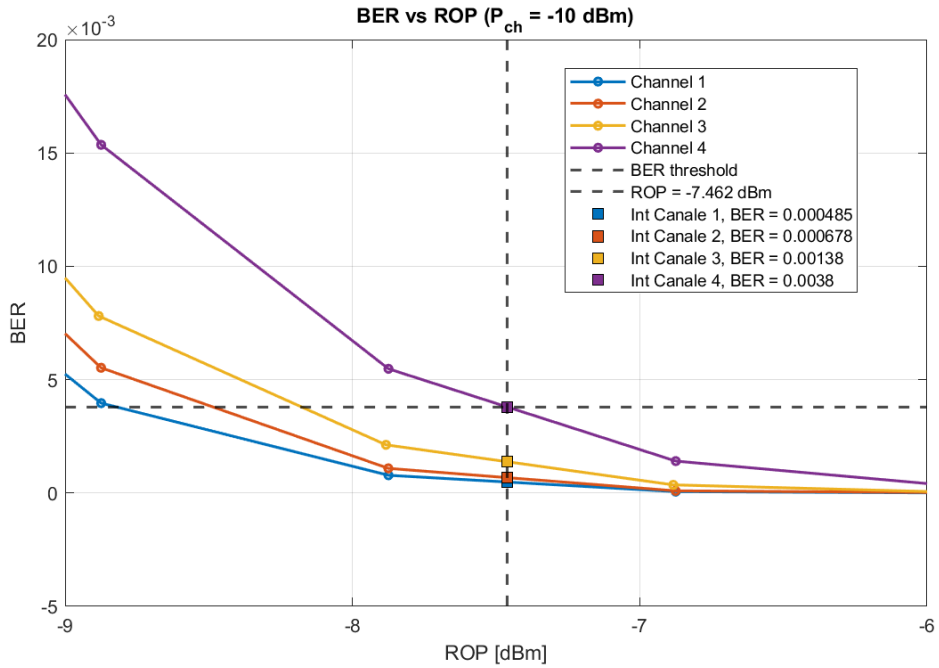

Figure 6.1: The ROP calculated at the BER target for the worst-performing channel, which in this case is channel 4.

with a central frequency corresponding to 1310 nm and a frequency shift of -3 THz. The simulation starts with analyzing the plot of BER vs ROP and taking into consideration the ROP value of the worst channel at BER target.Among all channels, the worst performing one determines the ROP necessary to guarantee acceptable performance for all the channels. Fixing the ROP at this value enables a detailed inspection of the signal through eye-diagram analysis. Two scenarios are evaluated:

- Before equalization, to observe the raw signal degradation, both with and without DCF.
- After equalization, to assess the equalizer's ability to mitigate distortions, with and without DCF.

For this value of ROP, simulation for each channel to reach this value are started for four different cases:

- without equalization and without DFC
- without equalization and with DFC
- with equalization and without DFC
- with equalization and with DFC

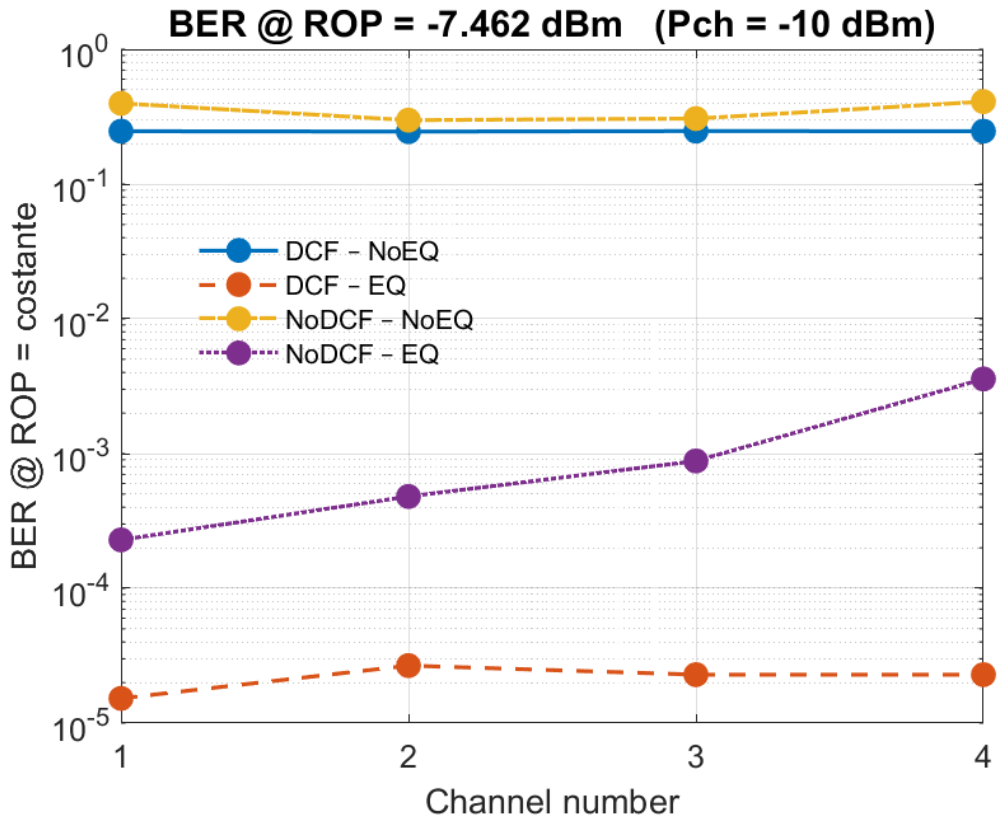

Figure 6.2: The transmission performance, evaluated in terms of BER at the target ROP for $P_{\text{ch}} = -10\,\text{dBm}$, is compared across four signal configurations: DCF with equalization, DCF without equalization, without DCF with equalization, and without DCF without equalization.

Interestingly, the configuration with DCF and with a simple FFE equalizer performs better than the transmission with equalizer and without DCF, where it is visible the effect of the chromatic dispersion in the performance of the different channels with Channel 4 worst than Channel 1. It is also really visible, figure 6.2, that the chromatic dispersion is completely compensated adding the DCF to the FFE equalizer and it can be deduced that the equalizer without DCF is able to perform well but because the system is has bandwidth limitations due to the frequency cut-off of the filter at the transmitter without compensating the Chromatic Dispersion. The initial expectation was that the DCF would strongly compensate chromatic dispersion, acting similarly to an equalizer and therefore reducing the received optical power (ROP) values. However, the results show that this is not the case: nonlinear effects and bandwidth limitation remain the dominant source of degradation, and DCF alone is insufficient to mitigate them in this configuration.

From the analysis of the transmission with a central frequency shift of -3 THz and

$P_{\text{ch}} = -10$ dBm over a 10 km fiber link, as shown in figures 6.1 and 6.2, it is evident that the worst performing channel is Channel 4, which requires a received optical power of ROP $= -7.46$ dBm to meet the BER target. The figures clearly show that transmission without equalization performs significantly worse than transmission with equalization, and that the inclusion of an ideal DCF does not yield a substantial improvement.

Interestingly, the configuration *without* DCF but equipped with a simple FFE equalizer performs noticeably worse than the case with DCF and equalization. The impact of chromatic dispersion is clearly visible in the degradation across the channels, with Channel 4 performing worse than Channel 1, as it accumulates the largest amount of dispersion due to the frequency shift of -3 THz from the central frequency at 1310 nm.

It is also evident that chromatic dispersion is fully compensated when the DCF is used together with the FFE equalizer, indicating that the equalizer alone is not sufficient to compensate dispersion.

The initial expectation was that the DCF would strongly mitigate both chromatic dispersion, acting similarly to an equalizer and thereby reducing the ROP. However, the results show that this assumption does not hold: nonlinear effects remain the dominant source of degradation, and DCF alone is insufficient to compensate them with this system.

The exact same test should be visible with the following eyediagrams for $P_{\text{ch}} = -10$ dBm, but due limited bandwidth of the filters both at the transmitter and at the receiver. As explained in section 1.2 there is a strong frequency cutoff especially in the lowpass filter of the transmitter which is 50GHz. In the following eyediagrams, figures 6.27, 6.28, 6.29, it is shown how the signal changes at different frequency cutoff of the ideal transmitter, with greater bandwidth the signal improves.

In the following eyediagrams it is shown how the signal changes at different frequency cutoff of the ideal transmitter, with greater bandwidth the signal improves. This behavior is shared also for the different launch powers and different laser linewidth used in the simulation without mainly differences between the different eyediagrams.

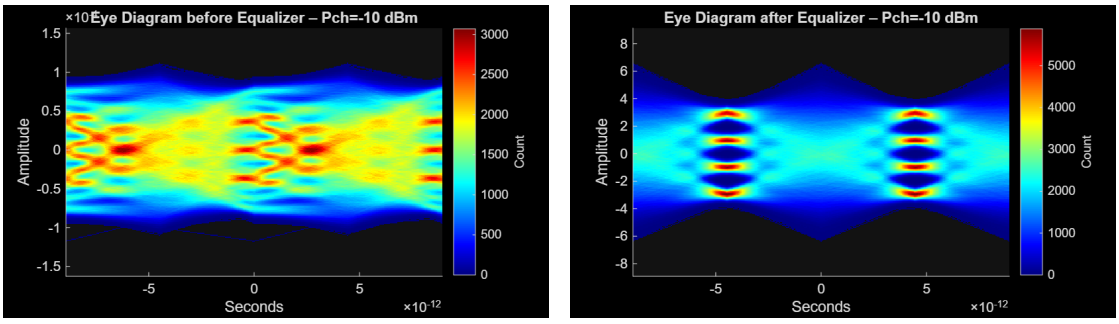

(a) Before FFE equalization

(b) After FFE equalization

Figure 6.3: Eye diagrams for Channel 1 at $P_{\text{ch}} = -10$ dBm without DCF.

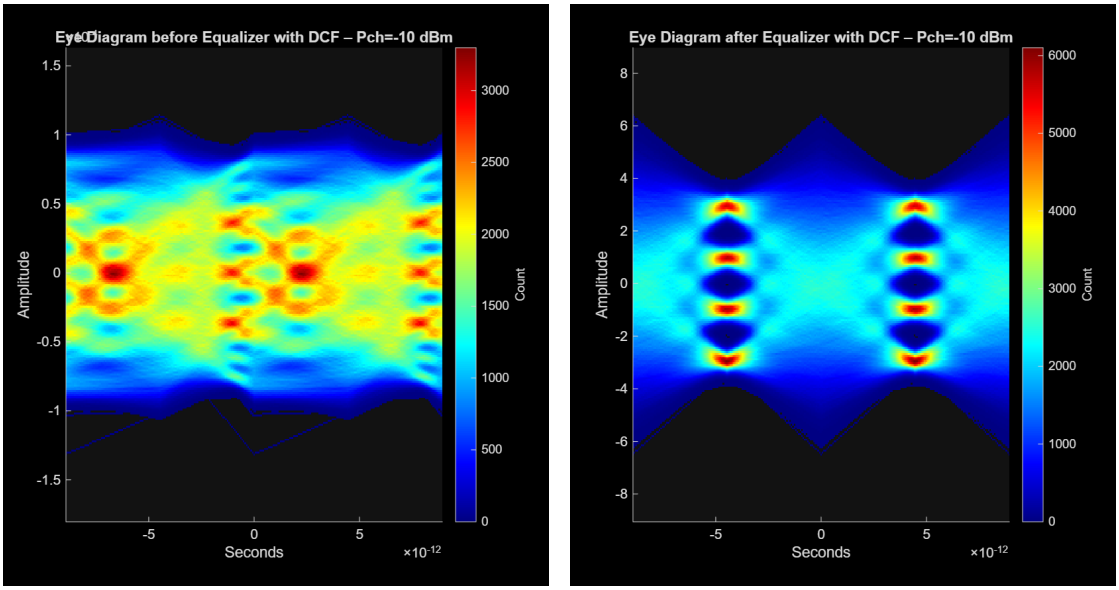

(a) Before FFE equalization (b) After FFE equalization

Figure 6.4: Eye diagrams for Channel 1 at $P_{\text{ch}} = -10$ dBm with DCF.

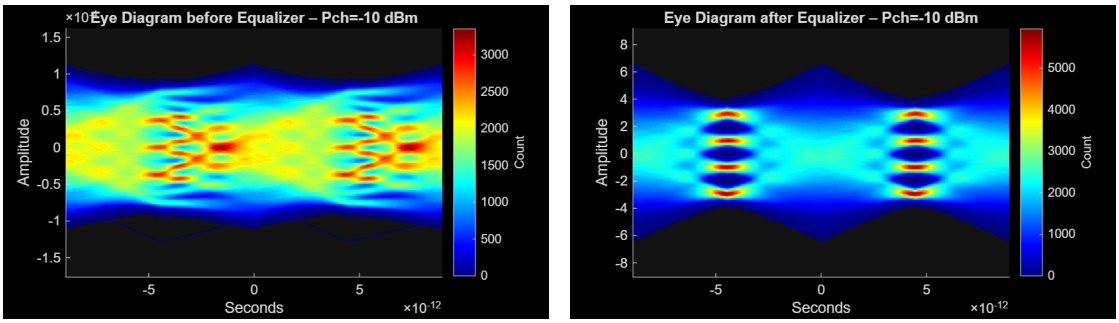

(a) Before FFE equalization (b) After FFE equalization

Figure 6.5: Eye diagrams for Channel 4 at $P_{\text{ch}} = -10$ dBm without DCF.

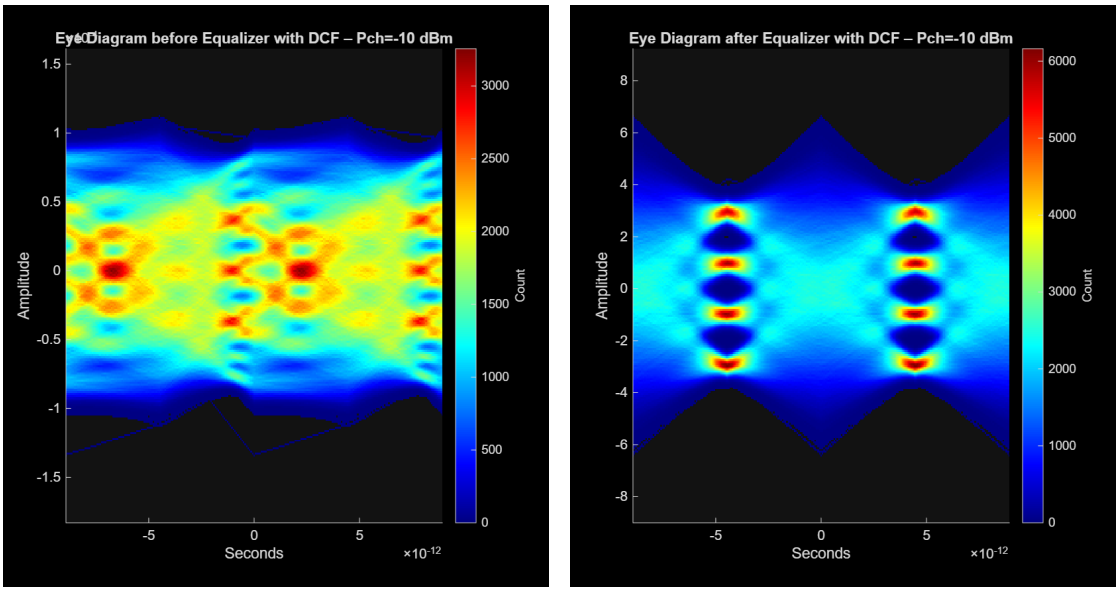

(a) Before FFE equalization (b) After FFE equalization

Figure 6.6: Eye diagrams for Channel 4 at $P_{\text{ch}} = -10$ dBm with DCF.

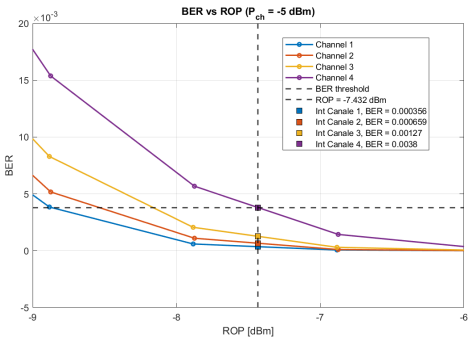

BER vs ROP

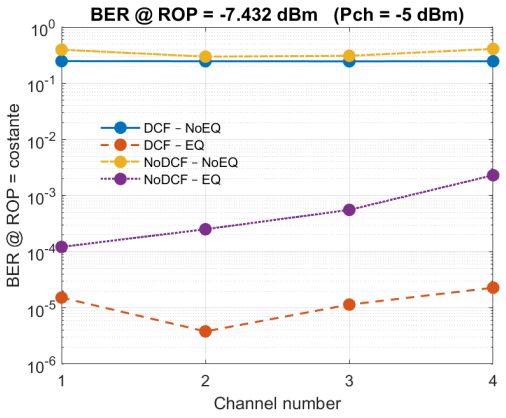

BER @ ROP target vs Channel frequency

Figure 6.7: Performance analysis of Equalizer with and without DCF at the worst channel ROP at target BER

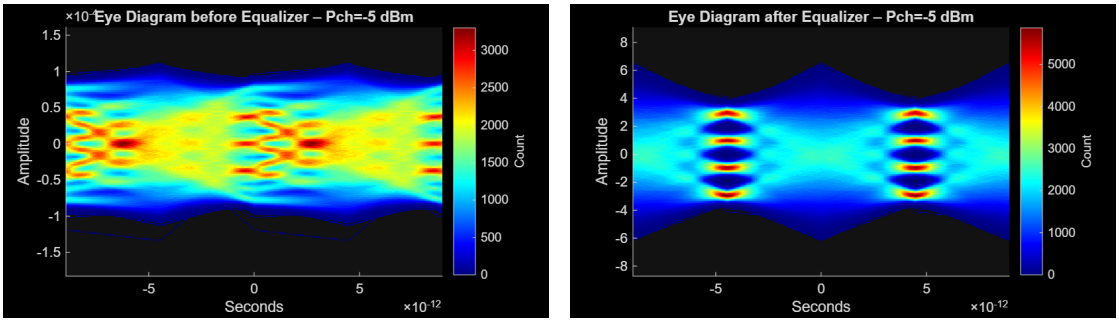

(a) Before FFE equalization (b) After FFE equalization

Figure 6.8: Eye diagrams for Channel 1 at $P_{\text{ch}} = -5$ dBm without DCF.

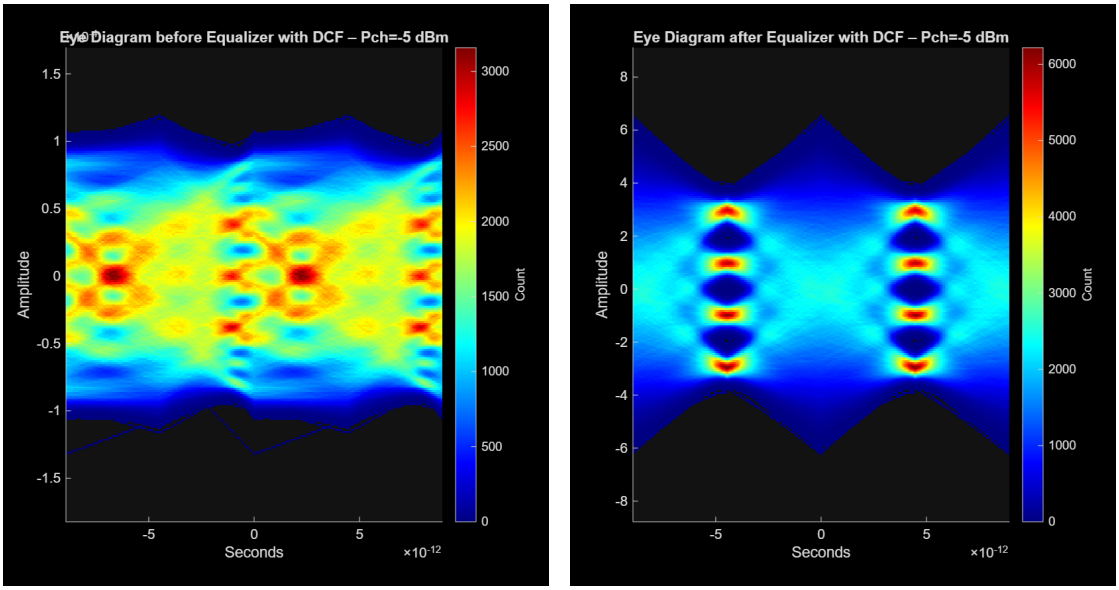

(a) Before FFE equalization (b) After FFE equalization

Figure 6.9: Eye diagrams for Channel 1 at $P_{\text{ch}} = -5$ dBm with DCF.

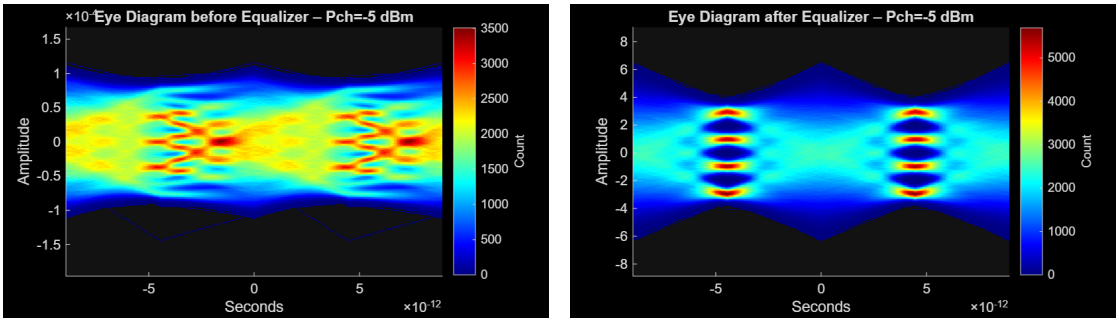

(a) Before FFE equalization (b) After FFE equalization

Figure 6.10: Eye diagrams for Channel 4 at $P_{\text{ch}} = -5$ dBm without DCF.

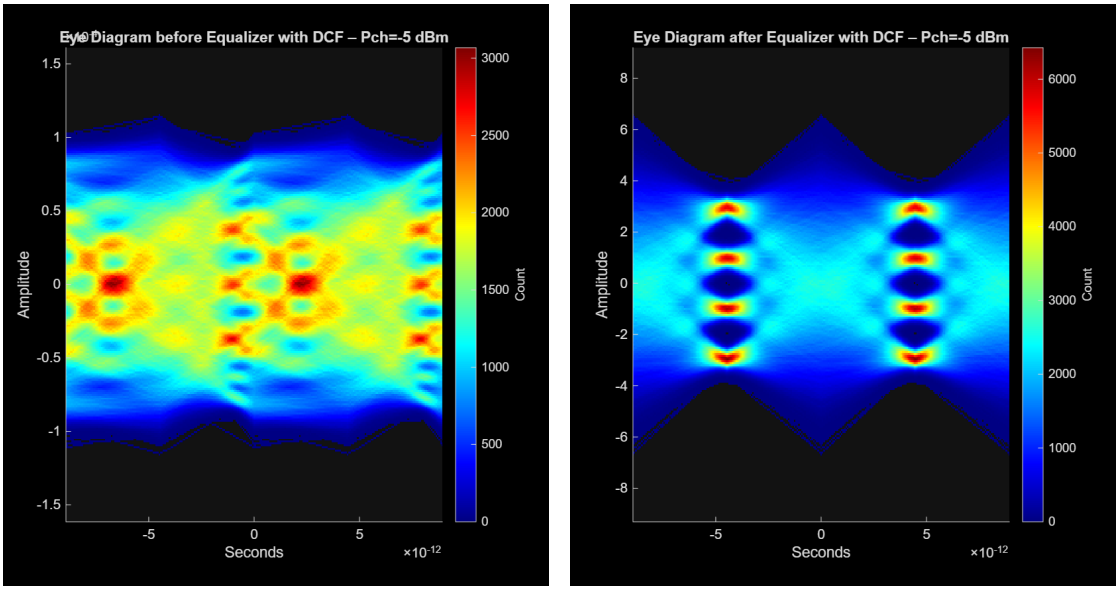

(a) Before FFE equalization (b) After FFE equalization

Figure 6.11: Eye diagrams for Channel 4 at $P_{\text{ch}} = -5$ dBm with DCF.

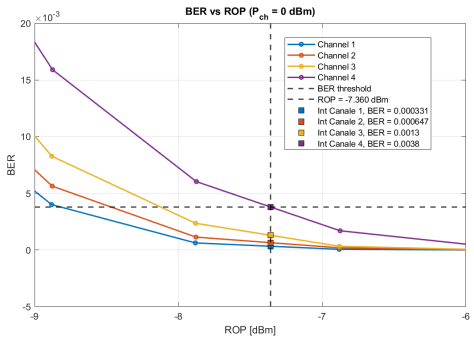

BER vs ROP

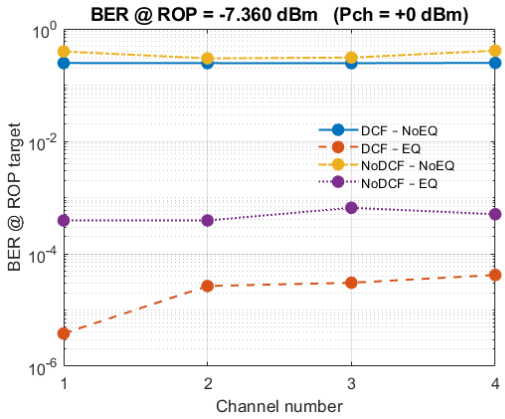

BER @ ROP target vs Channel frequency

Figure 6.12: Performance analysis of Equalizer with and without DCF at the worst channel ROP at target BER

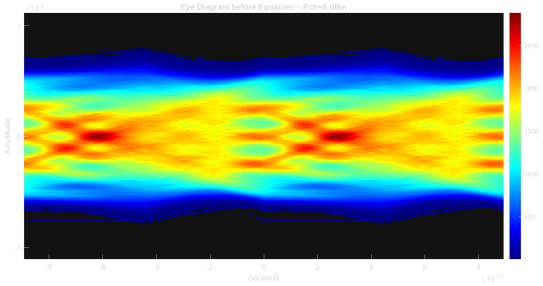

(a) Before FFE equalization

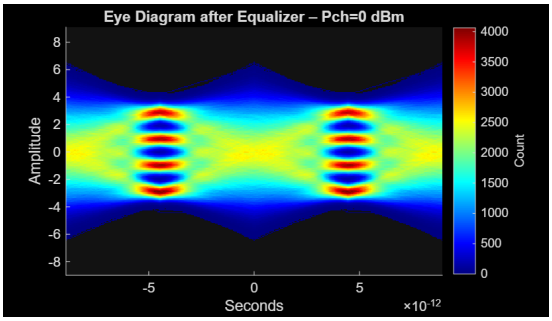

(b) After FFE equalization

Figure 6.13: Eye diagrams for Channel 1 at $P_{\text{ch}} = 0$ dBm without DCF.

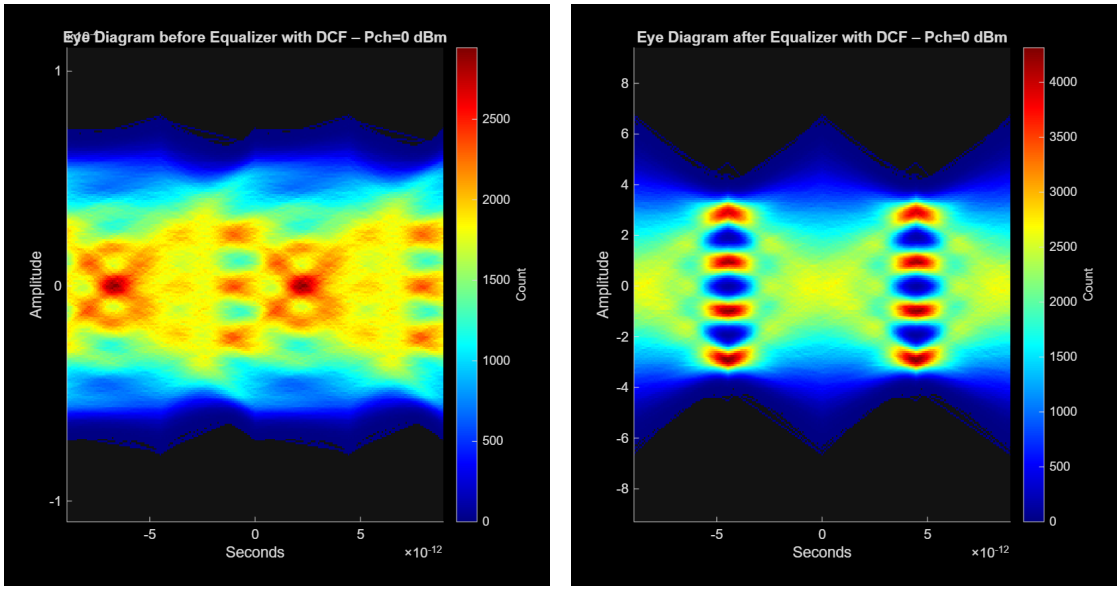

(a) Before FFE equalization (b) After FFE equalization

Figure 6.14: Eye diagrams for Channel 1 at $P_{\text{ch}} = 0$ dBm with DCF.

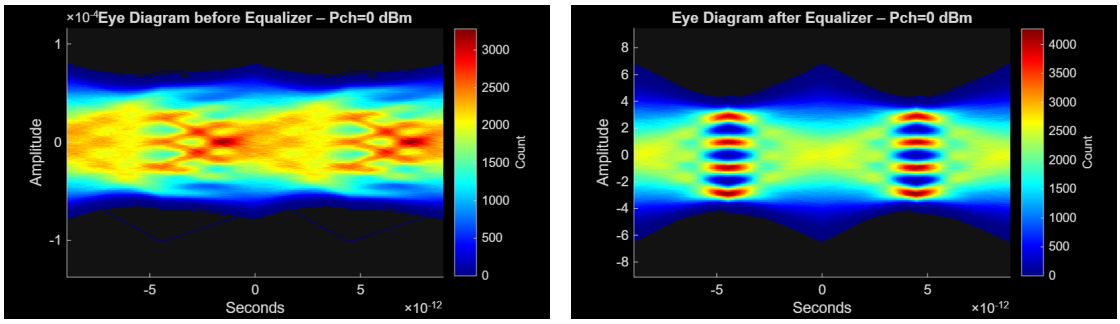

(a) Before FFE equalization (b) After FFE equalization

Figure 6.15: Eye diagrams for Channel 4 at $P_{\text{ch}} = 0$ dBm without DCF.

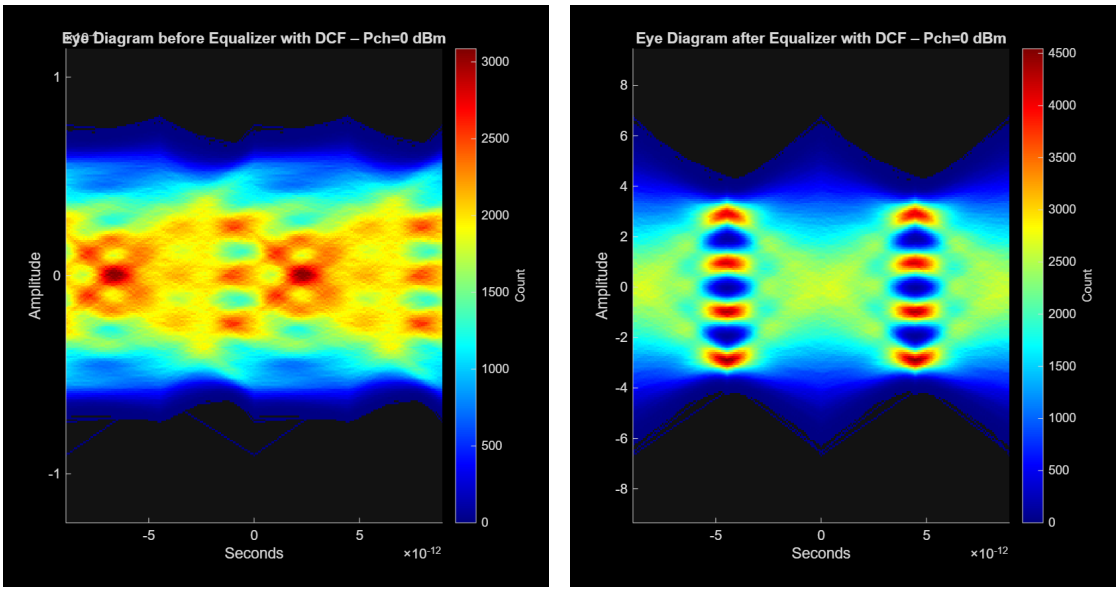

(a) Before FFE equalization (b) After FFE equalization

Figure 6.16: Eye diagrams for Channel 4 at $P_{\text{ch}} = 0$ dBm with DCF.

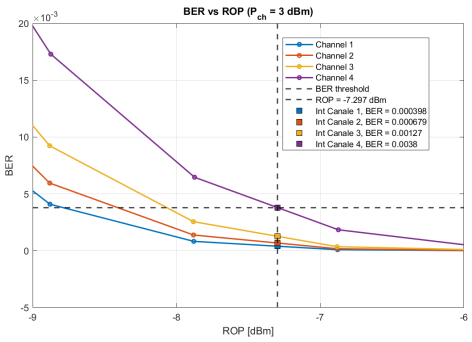

BER vs ROP

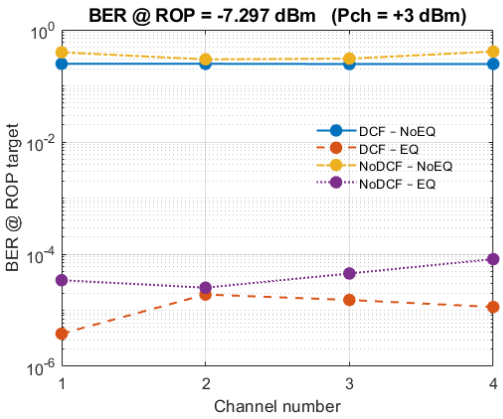

BER @ ROP target vs Channel frequency

Figure 6.17: Performance analysis of Equalizer with and without DCF at the worst channel ROP at target BER

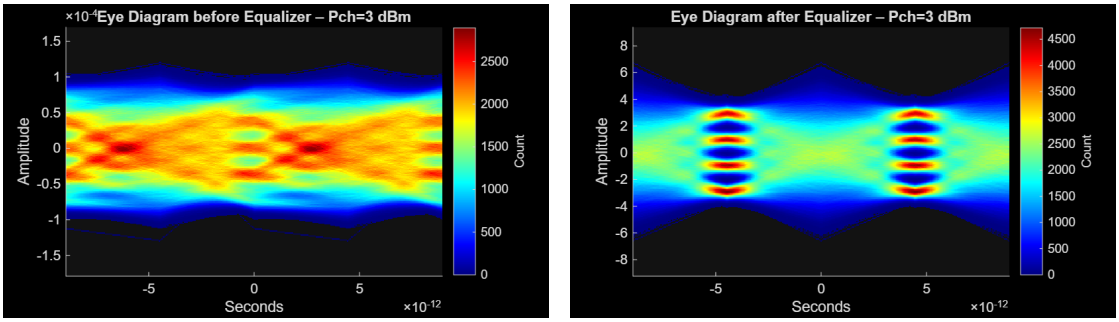

(a) Before FFE equalization (b) After FFE equalization

Figure 6.18: Eye diagrams for Channel 1 at $P_{\text{ch}} = 3$ dBm without DCF.

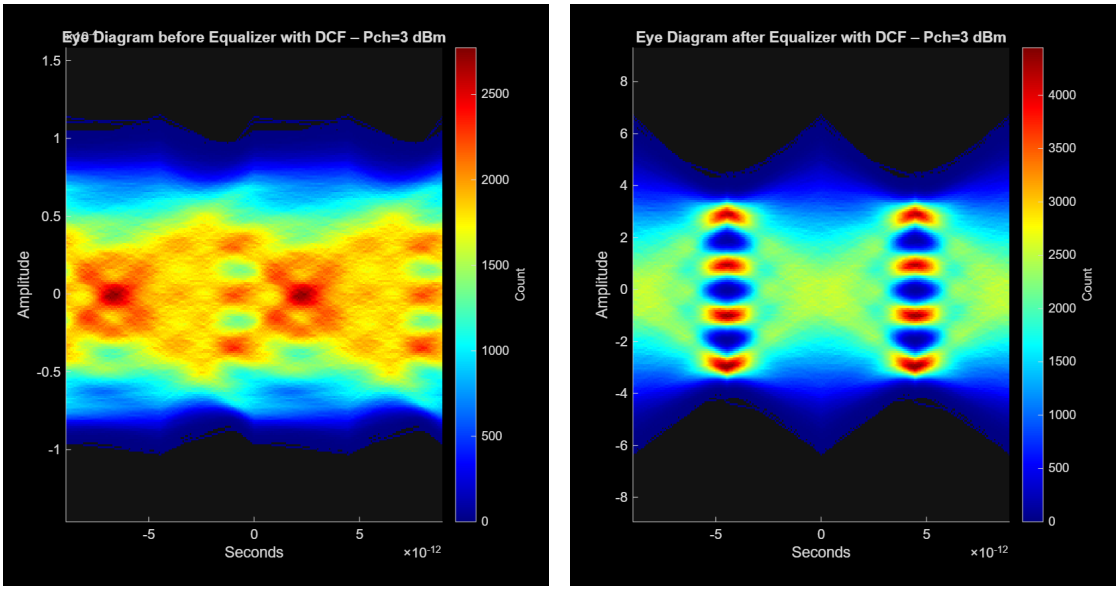

(a) Before FFE equalization (b) After FFE equalization

Figure 6.19: Eye diagrams for Channel 1 at $P_{\text{ch}} = 3$ dBm with DCF.

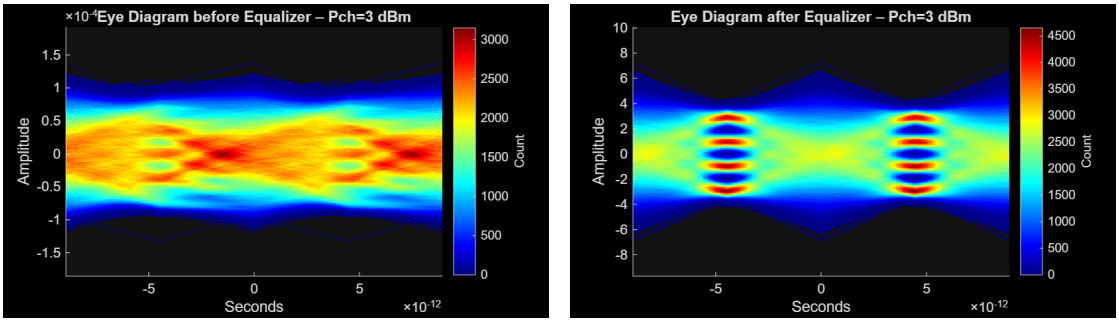

(a) Before FFE equalization (b) After FFE equalization

Figure 6.20: Eye diagrams for Channel 4 at $P_{\text{ch}} = 3$ dBm without DCF.

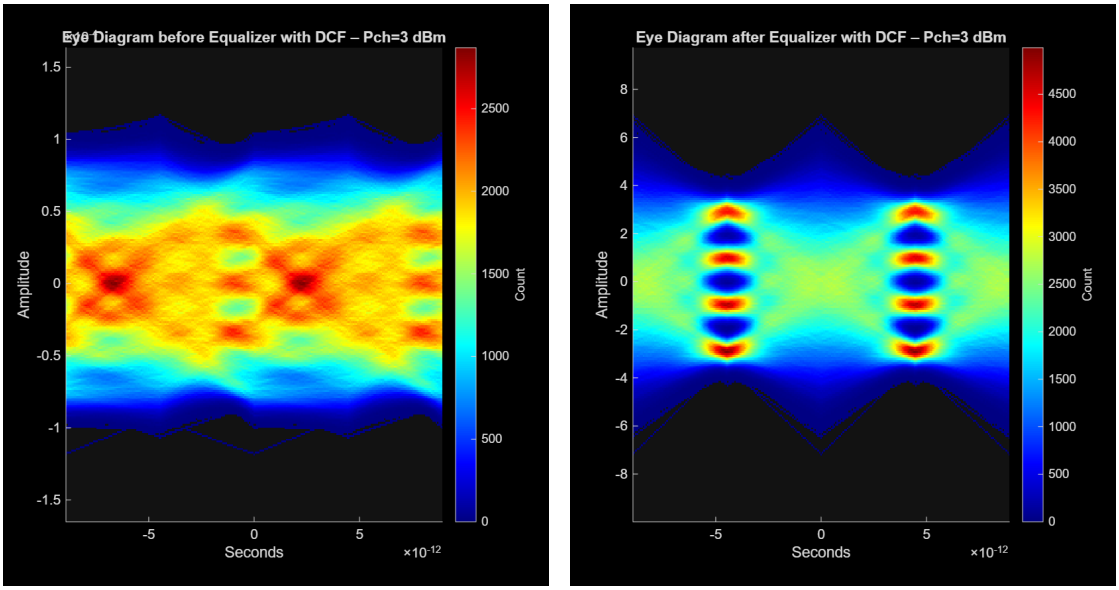

(a) Before FFE equalization (b) After FFE equalization

Figure 6.21: Eye diagrams for Channel 4 at $P_{\text{ch}} = 3$ dBm with DCF.

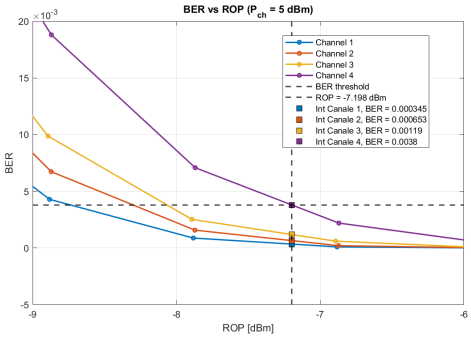

BER vs ROP

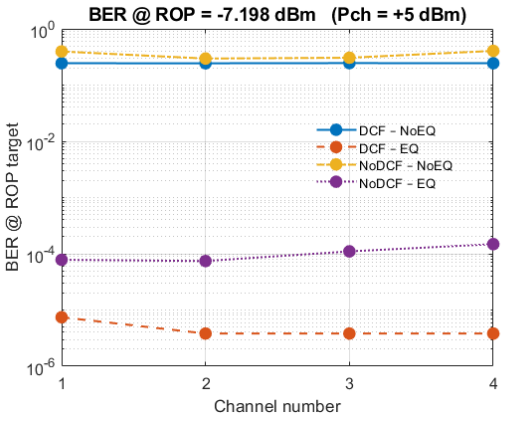

BER @ ROP target vs Channel frequency

Figure 6.22: Performance analysis of Equalizer with and without DCF at the worst channel ROP at target BER

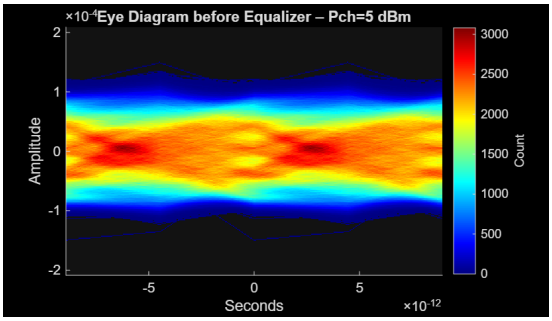

(a) Before FFE equalization

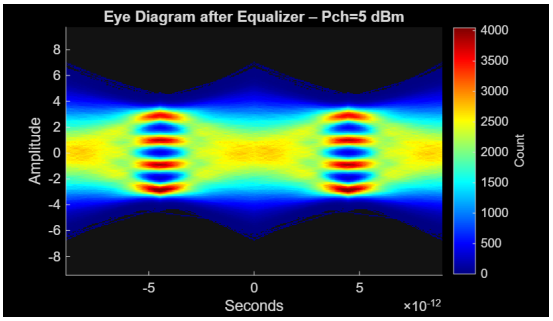

(b) After FFE equalization

Figure 6.23: Eye diagrams for Channel 1 at $P_{\text{ch}} = 5$ dBm without DCF.

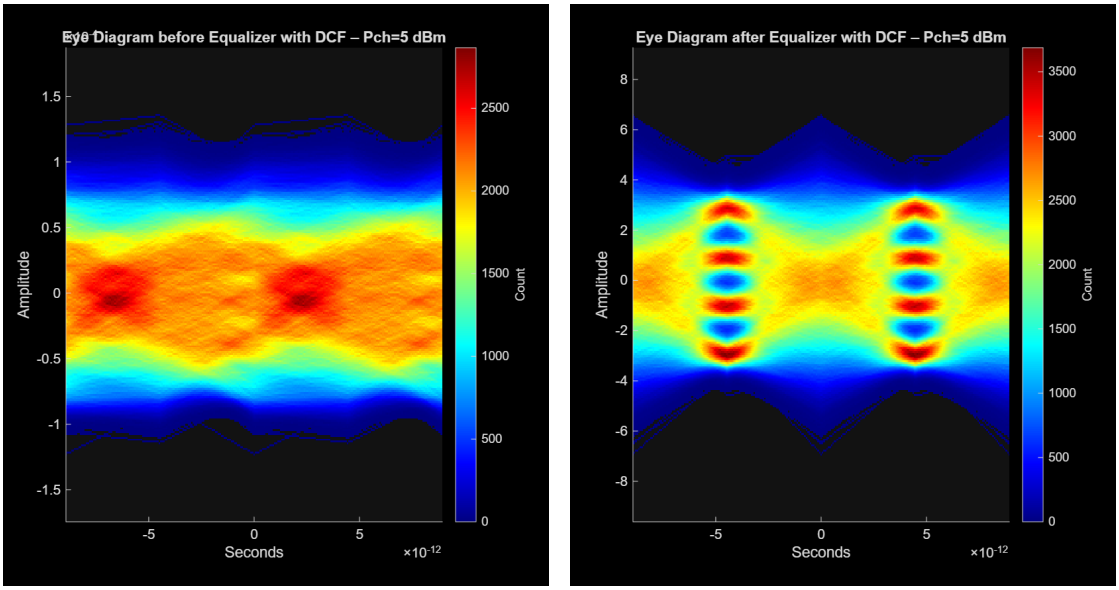

(a) Before FFE equalization (b) After FFE equalization

Figure 6.24: Eye diagrams for Channel 1 at $P_{\text{ch}} = 5$ dBm with DCF.

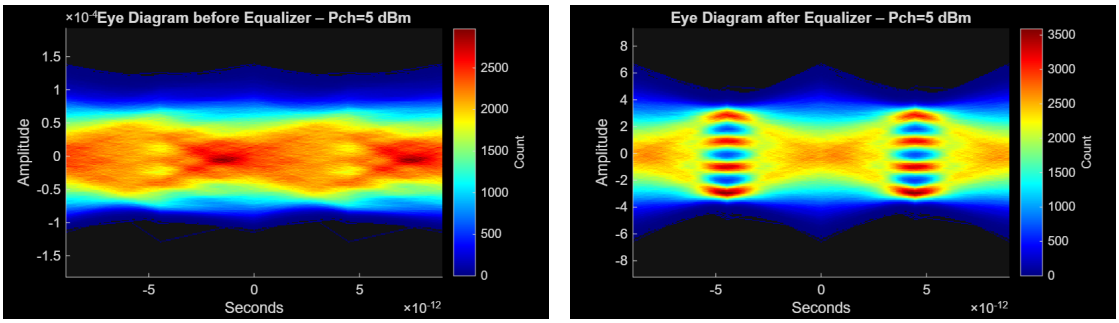

(a) Before FFE equalization (b) After FFE equalization

Figure 6.25: Eye diagrams for Channel 4 at $P_{\text{ch}} = 5$ dBm without DCF.

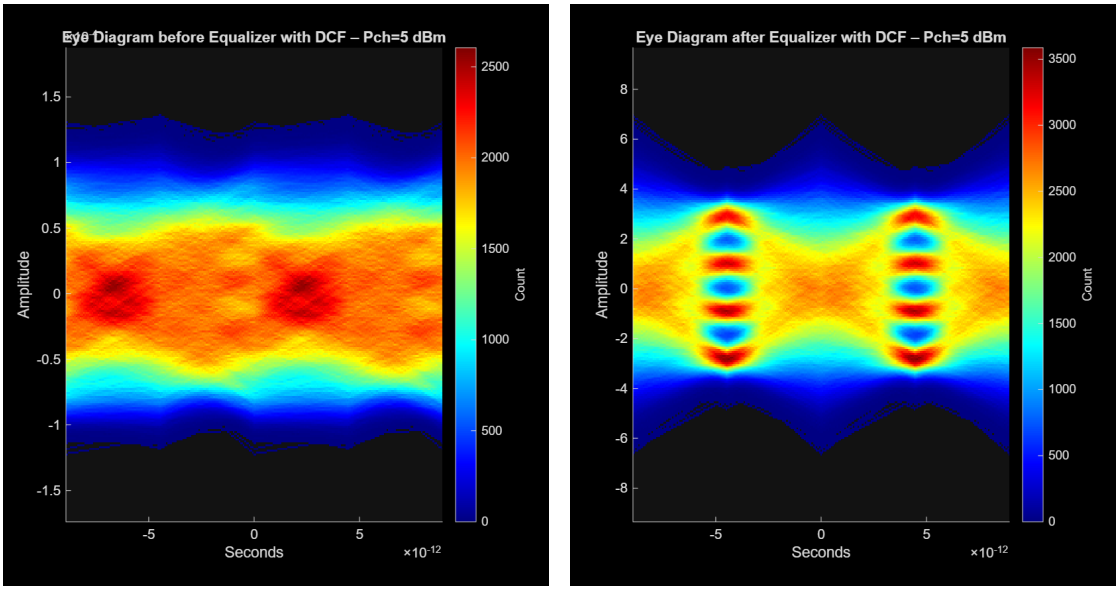

(a) Before FFE equalization (b) After FFE equalization

Figure 6.26: Eye diagrams for Channel 4 at $P_{\text{ch}} = 5$ dBm with DCF.

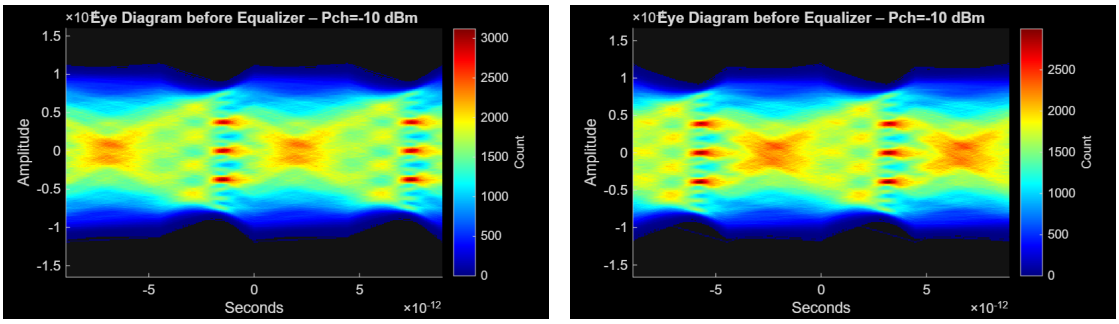

(a) Before FFE equalization channel 1 (b) Before FFE equalization channel 4

Figure 6.27: Eye diagrams for Channel 1 and Channel 1 at $P_{\text{ch}} = -10$ dBm with Transmission Bandwidth = 60 GHz

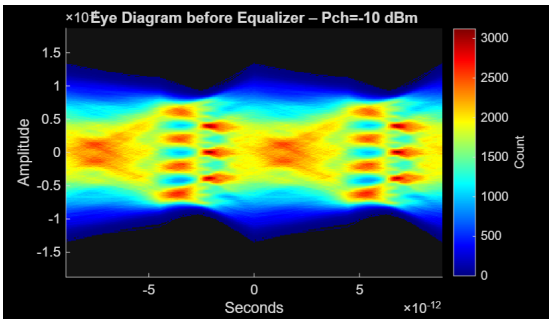

(a) Before FFE equalization channel 1

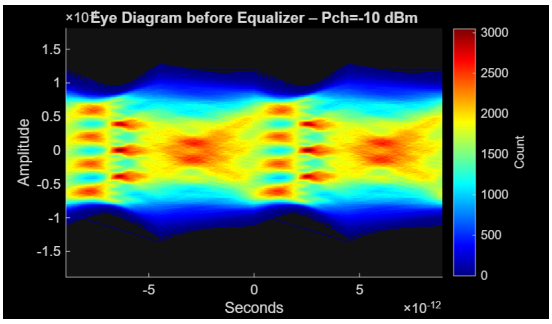

(b) Before FFE equalization channel 4

Figure 6.28: Eye diagrams for Channel 1 and Channel 1 at $P_{\text{ch}} = -10$ dBm with Transmission Bandwidth = 70 GHz

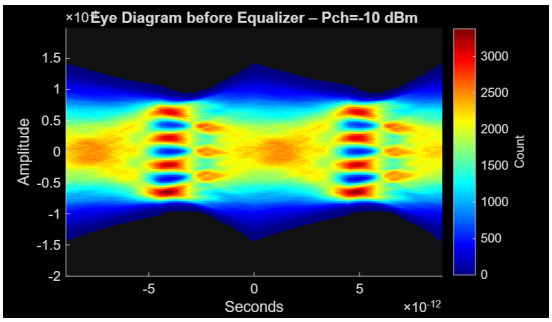

(a) Before FFE equalization channel 1

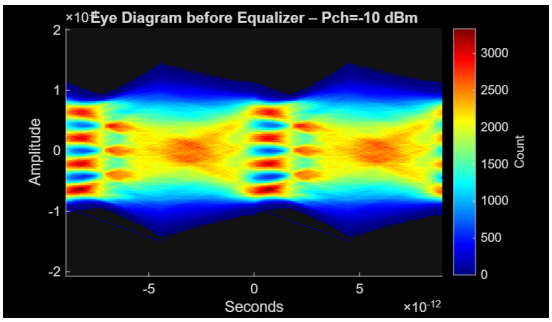

(b) Before FFE equalization channel 4

Figure 6.29: Eye diagrams for Channel 1 and Channel 1 at $P_{\text{ch}} = -10$ dBm with Transmission Bandwidth = 80 GHz

Chapter 7

Conclusion

This thesis begins with a brief overview of the current goals and research efforts trying to improve the performance of IM-DD technology in short reach optical systems. After a short introduction to IM-DD transmission, fiber propagation and the O-band, the simulator used to obtain the results presented in this work is described in detail. The second chapter provides the theoretical background, pexplaing IM-DD system and fiber propagation.

The main goal of the thesis is to analyze how IM-DD technology supports bit rates. However, operating at such high baud rates, the signal becomes more sensitive to linear and nonlinear impairments. The most relevant and impacting linear impairments is the chromatic dispersion, which is minimized in the O-band, but residual dispersion can still introduce inter-symbol interferences, especially working at this high symbol rates. The transmission is also affected by nonlinear Kerr effects and additional degradations can arise from the limited bandwidth of the transceiver and from the phase noise of the laser. The system is therefore analysed in detail to understand how all impairments affect signal quality.

The results show that the central frequency corresponding to the 1310 nm wavelength, the signal is unaffected by chromatic dispersion, whereas nonlinear effects due to the Kerr effect, in particularly FWM, become dominant. Shifting the central frequency away from the zero-dispersion point reduces the strength of FWM, but chromatic dispersion becomes the major limiting impairment. The laser linewidth has little impact when operating away from the zero dispersion wavelength,but at the ZDW its impact becomes significant,especially at higher launch powers.

To mitigate phase noise, residual dispersion and nonlinear Kerr effects, the optimal operating condition is identified as a moderate launch power combined with a small frequency shift (± 1 THz) from the zero dispersion point. To address chromatic dispersion, an additional investigation evaluates whether a DCF can compensate and separate linear and non linear elements. As demonstrated in the final chapter, the DCF alone cannot substitute a simple FFE equalizer because it cannot compensate nonlinearities added to the already present dispersion.

A robust approach to reduce nonlinear interference is the use of polarization configurations different from co-polarization, which reduces interferences and phase correlation between channels. Future work may explore the use of advanced DSP equalizers, using machine learning techniques, which can be capable of dynamically adapting filter coefficients to varying dispersion and ISI.

Bibliography

[1] G. P. Agrawal, 2013. 5th ed.

[2] IEEE P802.3df Task Force. 800 gb/s and 1.6 tb/s ethernet, 2023. Ongoing Standardization Project.

[3] Yang Hong, Kyle R. H. Bottrill, Natsupa Taengnoi, Naresh K. Thipparapu, Yu Wang, Jayanta K. Sahu, David J. Richardson, and Periklis Petropoulos. Numerical and experimental study on the impact of chromatic dispersion on o-band direct-detection transmission. *Applied Optics*, 60(15):4383–4390, 2021. Journal Article.

[4] IEEE. Ieee std 802.3bm-2015: 100 gb/s ethernet optical standards, 2015. Standard Specification.

[5] IEEE. Ieee std 802.3bs-2017: Media access control parameters for 200 gb/s and 400 gb/s ethernet, 2017. Standard Specification.

[6] IEEE. Ieee std 802.3cd-2018: Media access control parameters for 50 gb/s, 100 gb/s, and 200 gb/s ethernet, 2018. Standard Specification.

[7] IEEE. Ieee std 802.3cu-2021: 100 gb/s and 400 gb/s over single-mode fiber, 2021. Standard Specification.

[8] J. F. Nagel et al. Scaling ethernet to 800g and beyond. In *Proceedings of the Optical Fiber Communication Conference (OFC)*, San Francisco, CA, 2021. Conference Paper.

[9] Silas Oettinghaus, Talha Rahman, Tom Wettlin, Stefano Calabrò, Nebojsa Stojanovic, and Stephan Pachnicke. Link segmentation based nonlinearity reduction using fibers with shifted dispersion zero for datacenter networks. In *49th European Conference on Optical Communications (ECOC 2023)*, page 4, Glasgow, UK, October 2023. IEEE.

[10] M. J. Potasek. Applications of the split-step fourier method to the nonlinear schrödinger equation, 1984. vol. 1, no. 1.

[11] Hao Shen and Frédéric Pétrot. Using amdahl's law for performance analysis of many-core soc architectures based on functionally asymmetric processors. In *Lecture Notes in Computer Science*, Grenoble, France, 2011. Springer. Conference Paper.

[12] Cisco Systems. Cisco global cloud index: Forecast and methodology 2016–2021, 2016. Industry Report.